MICROSTRUCTURE, PHASE STABILITY, AND MECHANICAL PROPERTIES OF NiAl ALLOYS CONTAINING Zr AND Si

BY

YONGJIN LIM

A DISSERTATION PRESENTED TO THE GRADUATE SCHOOL
OF THE UNIVERSITY OF FLORIDA IN PARTIAL FULFILLMENT
OF THE REQUIREMENTS FOR THE DEGREE OF
DOCTOR OF PHILOSOPHY

UNIVERSITY OF FLORIDA

1997

To Yon and Mins

ACKNOWLEDGMENTS

First, I would like to thank God Who has led me to this stage and Who gave me a strong faith that He is always watching me whenever I struggle and need him. I also thank my advisor, Dr. Kaufman, who has always encouraged me. He has continually supported as I completed the degree and reminded me of why I am here. Also, I would like to thank all my committee members for helping me to finish this degree. I will never forget the great experimental help from Manas and helpful discussions with Dr. Ron Noebe at NASA. I would like to share this accomplishment with my wife and children.

TABLE OF CONTENTS

Page

ACKNOWLEDGMENTS ii

ABSTRACT v

CHAPTERS 1

1. INTRODUCTION 1

1.1 Background 1
1.1.1 Gas Turbine Engine Development 1
1.1.2 High Temperature Structural Materials 3
1.1.3 NiAl for High Temperature Structural Applications 5
1.2 Objective and Approach 7

2. REVIEW OF THE LITERATURE 9

2.1 General Characteristics of NiAl 9
2.1.1 Phase Diagram and Crystal Structure 9
2.1.2 Defect Structure and Site Occupation 11
2.1.3 Diffusion 12
2.2 Mechanical Properties of NiAl 14
2.2.1 Slip Systems 14
2.2.2 Yield Strength 15
2.2.3 Ductility 15
2.2.4 Stoichiometry Effects 17
2.2.5 Creep Properties 18
2.3 Ternary Alloying Effect 21
2.3.1 Phase Equilibria 21
2.3.2 Microstructures 23
2.3.3 Mechanical Properties 29
2.3.4 Other Properties 36

3. EXPERIMENTAL 37

3.1 Alloy Preparation 37
3.1.1 Polycrystalline Alloys 37
3.1.2 Single Crystals 38

3.1.3 Orientation Measurements 40
3.2 Heat Treatments 41
3.3 Mechanical Testing 42
3.4 Characterization 43
3.4.1 Optical Microscopy 43
3.4.2 Transmission Electron Microscopy (TEM) 43

4. RESULTS AND DISCUSSION 45

4.1 Microstructural Evolution 45
4.1.1 Alloy Group 1 45
4.1.2 Alloy Group 2 57
4.1.3 Alloy Group 3 64
4.1.4 NZS 10030 alloy 71
4.1.5 Summary 75
4.2 Microstructure and Mechanical Properties of NZ and NZS 00030 Single Crystals 78
4.2.1 Single Crystal Characterization 78
4.2.2 Mechanical Properties 79
4.2.3 Summary 99
4.3 Phase stability 99
4.3.1 G phase Stability in the NZS 10030 Alloy 100
4.3.2 A Geometrical Approach on the Phase Diagram Considering Chemical Formula 107
4.3.3 Summary 116

5. SUMMARY 117

APPENDIX A 119

APPENDIX B 121

REFERENCES 126

BIOGRAPHICAL SKETCH 132

Abstract of Dissertation Presented to the Graduate School
of the University of Florida in Partial Fulfillment of the
Requirements for the Degree of Doctor of Philosophy

MICROSTRUCTURE, PHASE STABILITY, AND MECHANICAL PROPERTIES OF NiAl ALLOYS CONTAINING Zr and Si

By

Yongjin Lim

May, 1997

Chairman: Dr. Michael J. Kaufman
Major Department: Materials Science and Engineering

A systematic study of microstructure evolution, phase stability, and mechanical properties in NiAl alloys containing Zr and Si was conducted. The study was based on the premise that fine, stable second phase precipitates in NiAl should increase its otherwise very poor creep strength. Three groups of alloys with varying Ni/Al and Zr/Si ratios, and total solute (zirconium and silicon) contents were prepared in order to determine experimentally the phase equilibria and microstructural evolution in the Ni-Al-Zr-Si quaternary system. Based on preliminary screening of polycrystalline alloys, two <001> single crystals were grown. The high temperature compressive strength of these single crystal alloys with different microstructures was measured at 1300 K, and was compared with that of Hf and Si modified NiAl alloys from previous studies. Microstructural analysis was performed by optical microscopy and transmission electron microscopy.

Three distinct phases--$Ni_{16}Zr_6Si_7$ (G), NiZrSi (E), and Ni_2AlZr (Heusler)--were observed in the Ni-Al-Zr-Si quaternary system, consistent with the Ni-Al-Hf-Si system, depending upon composition and heat treatment. It was observed that, for a given Zr/Si ratio, the alloy has a tendency towards increasing solubility of these elements with increasing Ni/Al ratio. For the alloys in which G phase was observed, both fine, cuboidal and coarser, plate-shaped precipitates developed depending on cooling rate. Finally, G phase was observed to be metastable in all cases except in the Ni-48.5Al-0.3Zr-0.25Si alloy which had a low volume fraction of the stable G phase. The high temperature strengths at 1300K and $10^{-4}s^{-1}$ ranged from 120 MPa (coarse E phase) to 350MPa (fine G phase) with the Heusler-containing material having intermediate strength. Precipitation hardening due to the fine cuboidal G phase was shown to be the major factor in enhancing the high temperature strength and zirconium appears to be as effective as hafnium in these alloys. The metastability of the G phase leads to flow softening in the Ni-49.5Al-0.3Zr-0.25Si single crystal deformed at 1300 K. Dislocation analyses performed after different levels of strain (softening) and stress exponent values (~5) indicate that <100> dislocations are dominant. Simple diagram constructions were developed using certain geometrical considerations and were used to suggest alloying strategies for producing stable β+G phase microstructures and resulting alloys were consistent with these predictions.

CHAPTER 1
INTRODUCTION

1.1 Background

1.1.1 Gas Turbine Engine Development

The increasing demands of turbine engines that power high performance military and commercial aircraft, as well as industrial turbines, have motivated a search for new materials. Typically, gas turbine engine materials are exposed to extremely severe environments: operating temperatures are high (up to 1000°C typically), the engine is operated cyclically between high temperature and room temperature, and the combustion gases are highly corrosive. Therefore, turbine engine design is strongly dependent on the development of materials that can withstand such aggressive environments.

The aircraft engine was developed by Frank Whittle of Great Britain and Han von Ohain in Germany in 1937. Their engines led to successful jet-powered fighter aircraft by the end of World War II. Figure 1-1 shows a typical modern jet engine. The basic components of the engine are the compressor, combustion chamber, driving turbine and exhaust duct. Figure 1-2 illustrates the engine components [1]. The compressor raises the pressure and temperature of the incoming air before passing it on to the combustion chamber (burner). In the combustion chamber, the air is mixed with fuel and burned. The heated gases are directed to the engine where they expand and perform work by rotating the turbines. The turbine rotates at speeds up to 11,000 revolutions per minute and provides the torque to drive the compressor. The exhaust gases expand through a nozzle to form a high velocity jet creating the thrust to propel the aircraft.

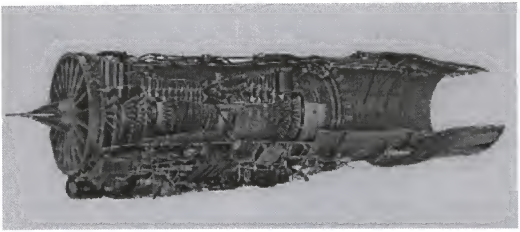

Figure 1-1. FW-100 jet engine (Courtesy of the Pratt & Whitney)

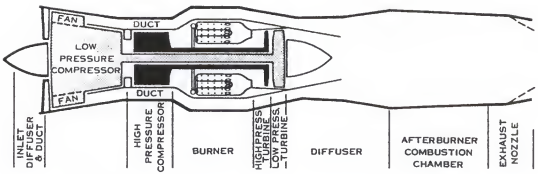

Figure 1-2. An aircraft turbine engine showing the basic components.

The theoretical efficiency of an ideal turbine engine with no internal losses depends only the ratio of the pressure in the compressor to the pressure in the atmosphere. One might think that the most obvious way to increase the efficiency in a turbine engine is to increase the pressure in the compressor. However, in a real turbine engine, increased pressures drastically increase both internal losses and the weight of the engine. Therefore, increasing the pressure beyond a certain point actually reduces efficiency. Significant improvements in turbine efficiency can also be obtained by

increasing the temperature of the gases in the combustion chamber. For best performance, the burning temperature should be as high as possible in order to effect complete combustion of the fuel-air mixture. Realistically, the temperature is limited since the first stage rotor blades in the turbine engine must be able to function at the high temperatures produced during combustion. Thus, substantial increases in turbine engine efficiency rely on materials that maintain their strength at higher temperatures. Even with complex air cooling around the turbine blades, the properties of available materials limit current turbine inlet temperatures to approximately 1100°C. The development of new, efficient turbine engines depends on the availability of new materials that are strong, lightweight and able to withstand the higher temperatures and stresses in the engine.

1.1.2 High Temperature Structural Materials

Ni-base superalloys have been the primary alloys of choice for high temperature structural applications since their debut in the late 1930s [2]. Ni_3Al (γ') precipitates that are coherent with the nickel-rich matrix are the major source of strengthening in most superalloys. The coherent boundaries between the matrix and precipitates present a continuous path for dislocation movement through the crystal so that the motion of dislocations through the particles produces anti-phase boundaries and superdislocations. The γ' phase is stable at high temperatures and its strength tends to increase with temperature, producing attractive high temperature properties, while the Ni matrix allows for sufficient low temperature ductility. The properties of Ni-base superalloys have made them the principal high temperature structural material for the past five decades. Significant improvements in their strength have been made through alloying and processing, i.e., directional solidification and single crystal growth. Modern nickel based superalloys are quite sophisticated, containing many alloy additions and special heat treatments to produce superior high temperature strength and environmental resistance.

This has allowed the operating temperatures to approach the incipient melting point of the alloys and, therefore, further improvements are not possible. Therefore, next-generation engine designs require materials with temperature capabilities beyond those of superalloys. Various candidate materials [3] have been examined for this purpose including refractory metals, ceramics, oxide dispersion strengthened (ODS) alloys, and intermetallic alloys.

Refractory metals (molybdenum, tungsten, niobium, etc.) were an early candidate for turbine engine materials due to their high melting temperatures and good strength at high temperatures. However, their poor oxidation resistance has been a major obstacle for this class of materials. While alloying additions and protective coatings have been used to overcome this challenge, the enhancements have been insufficient for the desired behavior [4].

The application of mechanical alloying techniques to superalloys led to what are now called oxide dispersion strengthened (ODS) superalloys. The resulting fine oxide particles distributed throughout the metal matrix provide effective barriers to dislocation motion. Furthermore, these oxides tend to remain stable with respect to coarsening at high temperatures. Although high temperature strength is significantly improved, the oxide dispersion tends to embrittle the alloy at low and intermediate temperatures. While some ODS alloys have been employed in high temperature applications, their low toughness has prevented them from becoming competitive with other high temperature structural materials [5].

Excellent heat resistance coupled with low density and oxidation resistance in covalently bonded ceramic materials offer many useful properties for high temperature applications [6]. Although ceramics maintain high compressive strength at high temperatures, they are extremely brittle in tension; this lack of toughness continues to preclude their application in most turbine components.

For many years, the beneficial effects of long-range order on strength has created an interest in the possible application of intermetallic compounds in turbine engines. Among the intermetallics, the aluminides tend to have the additional advantage of high oxidation resistance resulting from the protective nature of the alumina films. Much of the seminal work on aluminides has been performed on Ni_3Al (γ'), the major strengthening phase in superalloys, which displays an anomalous flow stress with increasing temperature. Besides Ni_3Al, considerable work has also been performed on other aluminides such as TiAl, Ti_3Al, FeAl, CoAl, and NiAl. While titanium aluminides have seen the most widespread application at intermediate temperatures, NiAl has also undergone considerable scrutiny in order to overcome its intrinsic drawbacks.

1.1.3 NiAl for High Temperature Structural Applications

Of the many intermetallics available, the B2 NiAl compound has many advantages as a promising high temperature structural material. These advantages include its ease of production, low density (~2/3 that of superalloys), high thermal conductivity (5 to 8 times higher than superalloys), and high melting point (~1950K) [7, 8]. However, there are two primary drawbacks: low toughness at ambient temperatures and low strength at all temperatures. These have limited its use for structural applications even though NiAl has been used for years as an oxidation resistant coating on turbine blades [9].

Microalloying NiAl with iron, molybdenum, and gallium in the 0.1-0.2 percent range has been shown to increase the ambient temperature ductility of soft-oriented single crystals. However, the mechanism for this effect has not been determined although it has been speculated that it is the result of gettering of interstitials [10]. In a recent study, Levit et al. [11] showed that approximately 20% elongation could be achieved in soft-oriented high purity NiAl single crystals; even so, the fracture still occurred by brittle cleavage. Thus, the low temperature toughness problem of NiAl remains to be solved.

Several attempts [9, 12-20] to increase the creep strength of NiAl have been made which include compositing, precipitation hardening and solid solution hardening. The approach of compositing using dispersoids, particulates, whiskers or fibers has been limited due to thermal expansion coefficient mismatch problems and to drops in thermal conductivity. Solid-solution or precipitation hardening approaches could be advantageous in their ability to exclude these problems. In fact, recent studies have shown that microalloying NiAl with hafnium leads to creep strengths approaching first generation nickel-base superalloys such as NASAIR 100 [21]. The Heusler phase (Ni_2AlHf) expected from the phase diagram [22, 23] was believed to be the major precipitate contributing to high temperature strength. However, a fine and uniform distribution of $Ni_{16}Hf_6Si_7$ (G phase) precipitates was observed instead of the Heusler phase in the hafnium-doped NiAl single crystals [21, 24]. While no silicon was added intentionally, the unexpected silicon was picked up due to reactions with the crucible and the investment mold; this led to the preference for G-phase formation. The discovery of this phase provided the impetus for a study of the possible existence of other types of precipitates in the quaternary Ni-Al-Hf-Si system and the Laves NiHfSi (E phase) was subsequently observed in certain alloys [25]. Thus, three types of precipitates can exist in these near β-NiAl quaternary alloys depending on composition and temperature [26]. Likewise, when zirconium is substituted for hafnium in these alloys, the same types of precipitates form.

The observation of G phase in the hafnium-doped alloy and its resistance to coarsening created a controversy concerning what type of precipitate (H and/or G) was most effective for hardening NiAl assuming that precipitation hardening plays the major role. The strength enhancement was observed in the hafnium-doped NiAl alloy containing G phase which appears to support precipitation hardening, although no clear mechanism was suggested [21]. In addition to this, there was some discussion of whether solid-solution hardening is as important as precipitation hardening in these alloys. Recently,

Noebe et al. [27] reported the effect of hafnium in the GE D-176* alloy was due to its stabilizing effect of the <110> type dislocations and the reduction of <001> dislocations to climb. Although the strengthening mechanism in this alloy remains controversial, it is suspected that the fine cuboidal G phase precipitates play a major factor in strengthening at high temperature. There are several aspects supporting this hypothesis: (1) G phase is coherent with the matrix whereas the E and H phase are not, (2) the G phase has a higher volume fraction than the others in these alloys studied, (3) its size is very fine (~ 20 nm, for the cuboidal G). If this assumption is true and zirconium also can form G phase, it is expected that zirconium will also increase the strength of NiAl at high temperatures in spite of the fact that zirconium was largely neglected after GE showed that the hafnium-doped alloy was superior in strength [28]. Therefore, the conclusion that zirconium is inferior to hafnium may have been premature.

Till now, there has been no clear evidence of the role of G phase on the strengthening at high temperature due to both an ambiguity of its existence at the testing temperatures (1300, 1400 K) and the difficulty of isolating its effects from the other phases such as Heusler and E phase. In addition, whether the G phase is stable or metastable in the composition and temperature range of interest is unclear. Thus, a thorough study of both microstructural evolution and phase stability in near β Ni-Al-Zr-Si alloys and their effects on the mechanical properties in this class of alloys is needed and forms the basis of this dissertation.

1.2 Objective and Approach

The primary goals of this study were (1) to understand microstructural evolution and phase stability in near β-NiAl alloys containing small additions of zirconium and/or silicon, (2) to determine if zirconium is as effective as hafnium in enhancing the creep

* trade name of GE's hafnium doped-NiAl single crystal

strength, and (3) to examine the relative roles of precipitation hardening and solid-solution hardening in enhancing the high temperature strength. Since there was no quaternary (Ni-Al-Zr-Si) phase diagram available, three groups of alloys with varying Ni/Al and Zr/Si ratios, and total solute (zirconium and silicon) contents were prepared in order to determine experimentally the chemical composition ranges in which G phase could be formed and, if possible, to stabilize it. The rationale behind this choice was based on such factors as (1) NASA/GE's study [25] on the Hf/Si-doped NiAl alloys, which indicated that the type of precipitate was strongly dependent on the Hf/Si ratio, (2) NiAl's property sensitivity to stoichiometry (Ni/Al ratio), and (3) the location of each phase field in the phase diagram. Considering these factors, 8 alloys were prepared; after preliminary screening of these 8 alloys, two single crystals (Ni-49.45Al-0.3Zr-0.25Si and Ni-49.7Al-0.3Zr) were grown along <001>. The high temperature compressive strength of these single crystal alloys with different microstructures was measured at 1300 K and compared with that of the NiAl alloys doped with hafnium and silicon. The phase stability was determined on two alloys containing 50 nickel and 51 nickel with similar amounts of zirconium and silicon, since it was suspected that the ambiguity of the stability of G phase in the GE/NASA crystals was due to the different nickel contents resulting from aluminum evaporation during crystal growth.

CHAPTER 2
REVIEW OF THE LITERATURE

2.1 General Characteristics of NiAl

2.1.1 Phase Diagram and Crystal Structure

The Ni-Al equilibrium phase diagram is shown in Figure 2-1 [29]. NiAl exhibits a wide single phase field and the stoichiometric composition melts congruently at ~ 1911 K. Significant long range order has been observed up to the melting temperature in an investigation of the X-ray intensity of {100} superlattice peaks in single crystals of NiAl [30]. The strong attraction between Ni and Al determines many of the characteristic properties of NiAl.

NiAl has the B2 structure. The unit cell is shown schematically in Figure 2-2 [31] where it is clear that it is BCC-like with Ni at 0, 0, 0 and Al at 1/2, 1/2, 1/2. The B2 structure is stable for large deviations from stoichiometry and long range order is reported for both Ni-rich and Al-rich compositions [30, 32]. The lattice constant of the stoichiometric composition at room temperature is 0.2887 nm [33] and the variation of lattice parameter with respect to composition within the single phase region has been determined [33, 34]. A maximum in the lattice constant occurs at the stoichiometric composition and the decrease on either side is related to the defect structure as described below.

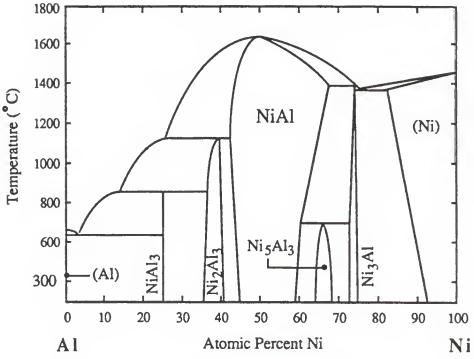

Figure 2-1. The Ni-Al equilibrium phase diagram [29].

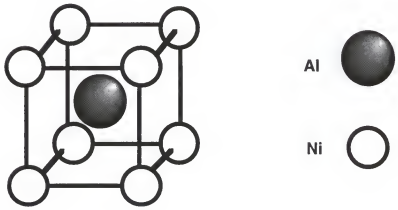

Figure 2-2. NiAl B2 structure [31].

2.1.2 Defect Structure and Site Occupation

Non-stoichiometric NiAl alloys must contain structural defects to accommodate the deviations from stoichiometry. These types of defects are referred to as constitutional defects and their nature is determined from measurements of the composition dependence of the lattice constant and density of NiAl (Figure 2-3) [33, 34]. Two types of structural defects have been suggested in NiAl according to the triple defect concept, namely Ni-vacancies and anti-site Ni atoms [35, 36]. Constitutional defects are reported to display short range order [37] such that there is a strong tendency to avoid the same species as first nearest neighbors [38]. Since Ni is smaller and heavier than Al, increasing the Ni content by substitution of Ni on Al sites should cause the lattice parameter to decrease and the density to increase, consistent with the data for Ni-rich alloys. However, the behavior for Al-rich alloys does not follow this trend. Instead, the lattice spacing of NiAl decreases and the decrease in density is more rapid than would be expected by the replacement of Ni atoms by aluminum. Consequently, the deviation from stoichiometry in Al-rich alloys is accommodated by the creation of vacancies on Ni sites instead of by substitutional Al anti-site defects as in the Ni-rich alloys. These constitutional defects significantly affect both the mechanical and physical properties of NiAl [39-42].

Since NiAl is strongly ordered, substitutional additions may exhibit certain site preferences which also strongly affect the mechanical properties [43]. This sensitivity of site preference on mechanical properties has been the driving force for site occupation studies. Several theoretical [44-46] and experimental [47-49] studies have been performed on ternary NiAl alloys. However, little work has been attempted concerning the role of defects, induced by site preference, on second phase formation in this compound. The point defects resulting from the site preference should affect the diffusion process which is an important factor in precipitation.

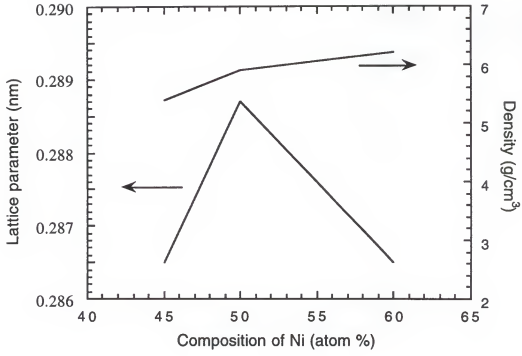

Figure 2-3. Composition dependence of the lattice constant and density of NiAl [33,34].

The site preference of elements in NiAl is shown in Table 2-1. Hosoda et al. [45] used bond strength calculations in order to predict that Zr and Hf have no site preference whereas Si prefers Al sites. On the other hand, Cotton et al. [47] classified both Hf and Si as preferring Al sites. In either case, it is believed that the addition of both Zr and Si in NiAl may generate constitutional defects by causing effective deviations from stoichiometry (Ni/Al ratio).

2.1.3 Diffusion

Although there is no unambiguous diffusion mechanism suggested [50-53], the importance of diffusion in describing high temperature deformation in NiAl is indicated

Table 2-1. The site preference of elements in NiAl [45].

1A	2A	3A	4A	5A	6A	7A	8A	1B	2B	3B	4B	5B
Li	Be											
Na	Mg									Al	Si	
K	Ca	Sc	Ti	V	Cr	Mn	Fe	Co	Ni	Cu	Zn	Ga	Ge	As
Rb	Sr	Y	Zr	Nb	Mo	Te	Ru	Rh	Pd	Ag	Cd	In	Sn	Sb
Cs	Ba	La	Hf	Ta	W	Re	Os	Ir	Pt	Au	Hg	Tl	Pb	Bi

Ni site Al-site(with structural defect) either site

by the correlation between the activation energy of diffusion and that for creep deformation [14, 54, 55]. The diffusivities of Ni, Al, and other elements in NiAl have been measured by using isotopes -^{63}Ni, ^{60}Co, and ^{114}In- as well as by studying diffusion couples. Since a stable isotope of Al is not readily available, the rate of diffusion of Al in NiAl is not well documented although diffusion models and experiments suggest that the difference in diffusion rate is not large between Al and Ni in NiAl. A minimum in the diffusion coefficient is reported for Ni-rich and Al-rich alloys near the stoichiometric composition. The activation energy for diffusion is greatest for the stoichiometric composition (307 ± 10 kJ/mol) [56], with a gradual decrease for Ni-rich compositions and a sharper drop for Al-rich compositions. The lower activation energy in Al-rich NiAl alloys is believed to correspond to the energy of motion of constitutional vacancies, while the higher activation energy for Ni-rich NiAl reflects the energy required to form and move a vacancy.

2.2 Mechanical Properties of NiAl

2.2.1 Slip Systems

In general, NiAl exhibits two significantly different types of slip behavior depending on crystal orientation. Crystals tested along <001> orientation have been designated as "hard" due to their high yield strength compared with crystals tested along non-<001> directions, which are generally referred to as "soft." The dominant slip vector for "soft" single crystal orientations and polycrystalline alloys is <001>. However, in the "hard" orientation, there is zero resolved shear stress (RSS) on <001> dislocations and the operative slip vector has been reported to be <111> at low and intermediate temperatures (<600K) and a combination of <110> and <100> at elevated temperatures (>600K).

Ball and Smallman [57, 58] were the first to identify the <001>{110} slip system in soft-oriented crystals tested between 300 and 1273 K. Wasilewski et al. [59] reported duplex cube slip <001>{100} in [110]-oriented single crystals; this was confirmed subsequently by Field et al. [60]. Cube slip was also observed in [112] crystals deformed between 77 and 1053 K. Due to the non-dissociated and compact nature of the <001> dislocation cores [61] , <001> dislocations are much more mobile than all other dislocations. The deformation behavior of polycrystalline alloys is consistent with the soft-orientation single crystals and both {110} and {100} slip planes have been reported [43, 62]. Isolated dislocation segments with non-<001> Burgers vectors have been observed in as-extruded NiAl [63, 64] probably due to the extensive deformation that occurs during the extrusion process [65]. However, the existence of non-<001> type dislocations in the polycrystalline NiAl does not suggest another deformation mechanism. The operation of <001> dislocations on planes other than {110} and {100} is not common, but reported under special conditions of constrained flow [66].

2.2.2 Yield Strength

Similar to BCC transition metals, the yield strength and flow behavior of NiAl are extremely sensitive to temperature and composition and exhibit a strong temperature dependence at low temperatures which has been attributed to a high Peierls stress. In <100>-oriented crystals, a yield stress plateau is observed at intermediate temperatures where the yield stress is only mildly temperature dependent; at high temperatures, the yield stress again drops with temperature. On the other hand, the strength gradually decreases with increasing temperature in non <001>-oriented crystals. Some results for single crystal and polycrystalline NiAl are shown in Figure 2-4 [67-70] where it is apparent that the yield stress of single crystals exhibits a strong dependence on orientation. The yield stress versus temperature curves for soft-orientation single crystals is similar to those observed for polycrystalline NiAl.

As noted above, at low temperatures, hard-oriented single crystals exhibit yield stresses several times greater than those for other orientations and a lower temperature dependence. When the temperature is increased above approximately 600 K, however, the yield stress of these crystals becomes extremely temperature dependent exhibiting a sharp decease in yield stress over a narrow temperatures range. In this regime, the slip vector has been shown to change from <111> to <001> and <011> [68]. Finally, at temperatures exceeding 1000 K, bulk diffusional processes dominate resulting in yield strengths similar to those observed in soft-oriented single crystals and in polycrystalline NiAl.

2.2.3 Ductility

Single crystals of nominally stoichiometric NiAl exhibit different behavior depending on crystallographic orientation. Hard-oriented single crystals exhibit essentially zero plastic strain to failure in tension at room temperature but undergo a sharp BDT (brittle-to-ductile transition) at temperatures near 600 K. Similarly, soft-oriented single

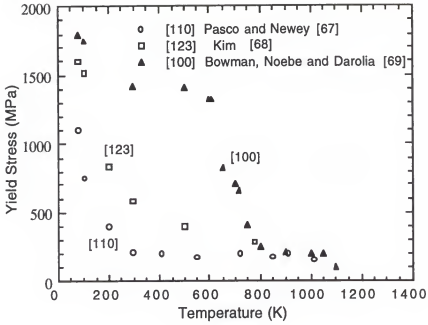

a)

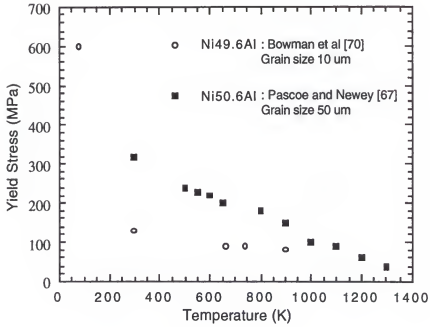

b)

Figure 2-4. Yield stress as a function of temperature for (a) single crystals in different orientations and (b) polycrystalline NiAl.

crystals also exhibit a sharp BDTT ranging from 475 to 525 K. In hard-oriented crystals, the BDTT corresponds to the steep decrease in yield stress with increasing temperature. This decrease has been attributed to a change from <111> slip to climb of <100> and <110> dislocations. Initially, it was reported that soft-oriented single crystals also exhibited extremely low plastic strains to failure at room temperature. Slightly above the BDTT, anomalously large tensile elongations (greater than 100 percent) have been reported for soft-oriented single crystals, while at even higher temperatures the ductility drops back down to approximately 45 percent. Takasugi et al. [71] attributed this increase to a balance between work hardening caused by glide and relaxation processes due to climb resulting in large resistance to necking. Most recently, Levit et al. [11] reported 24% elongation in prestrained NiAl at room temperature. However, the fracture mode did not change at all, i.e. it remained brittle.

2.2.4 Stoichiometry Effects

As mentioned above, deviations from exact stoichiometry affect the physical and mechanical properties of NiAl. Westbrook [31] first noted the effects of deviations from stoichiometry on mechanical properties by measuring the microhardnesses of various binary arc-melted alloys. Pascoe and Newey [67] more completely investigated the effects of composition on the flow behavior of NiAl and found that at low and intermediate temperatures, the minimum yield stress occurs in the stoichiometric alloy due to constitutional defect hardening on either side of stoichiometry. Ball and Smallman [58] found a reversion phenomenon at temperatures above approximately 800 K where the near-stoichiometric alloy has a higher initial flow stress than non-stoichiometric alloys (Figure 2-5). Since the activation energy for self-diffusion decreased with deviation from stoichiometry [52], the enhanced climb in the non-stoichiometric compositions leads to this reversion in flow stress at elevated temperatures.

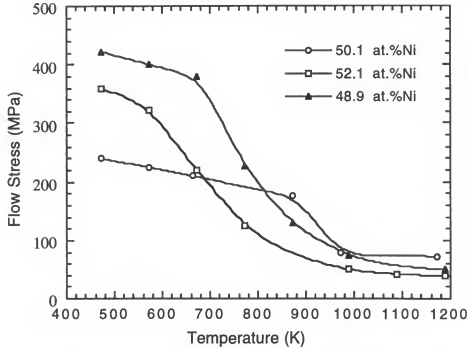

Figure 2-5. 0.2% Yield stress as a function of temperature for polycrystalline NiAl alloys with different stoichiometries [58].

2.2.5 Creep Properties

Creep resistance is one of the most important properties required for the extended use of NiAl at elevated temperatures. The second stage or steady-state creep rate, $\dot{\varepsilon}$, is usually expressed as a form of the Dorn equation: $\dot{\varepsilon} = A\,(\sigma/E)^n \exp(-Q/RT)$ where σ is the applied stress, E the Young's modulus, n the stress exponent, Q the activation energy for creep, R the gas constant, T the absolute temperature and A a constant which takes into account such variables as microstructure and stacking fault or anti-phase boundary energy. The values for n and Q are dependent on the operative deformation mechanism within a given temperature and stress regime and are thus useful indicators of the deformation mode. Knowledge of the diffusion behavior is desirable for understanding creep behavior since the value of Q_{creep} is often similar to that for diffusion, Q_D. From

previous diffusion studies, it appears that the activation energy for diffusion in binary NiAl is a maximum at the stoichiometric composition consistent with the diffusion coefficient minima. Although there is considerable scatter among the various diffusion data, the most likely range for Q_D is 250-300 kJ/mol [52, 72, 73]. The average value for the activation energy of creep is approximately 315 kJ/mol.

Dislocation creep in single phase metals and alloys can usually be classified as one of two main types: Class M for pure metal creep, and Class A for alloy behavior [74, 75]. Class M creep is characterized by glide being much faster than climb, and thus creep becomes controlled by the rate of dislocation climb past substructural obstacles. Class A creep is called viscous glide controlled creep since the glide of dislocations is restricted by solute atoms. This reduced mobility is the limiting creep process while climb can occur readily. These two types of behavior can be distinguished by several criteria including the shape of the primary creep curve, the stress exponent and the formation of a dislocation substructure.

Most of the stress exponents in NiAl obtained from various sources have similar values on the order of 4.5 to 6, except for a transition to a lower stress exponent at the lowest stress levels. Examination of the stress exponents for materials having a wide variety of grain sizes, including single crystals, reveals that between 1100-1400K, the values cluster between 5 and 7. Class A materials are usually characterized by a stress exponent of 3 while Class M display stress exponents of ~5. Although a stress exponent of 7 is higher than that characteristic for Class M behavior, such high values have been observed in several Class M materials. However, the characteristics in NiAl such as (1) observation of subgrain formation after high temperature deformation, (2) the operation of normal primary creep behavior, and (3) strengthening via a reduction in grain size are consistent with Class M behavior. Consequently, high temperature creep in binary NiAl is apparently climb controlled over most stresses and temperatures. Forbes et al. [55] have argued that creep deformation in single crystal NiAl is a mixture of both Class A and

M behavior depending upon both crystal orientation and the stress/temperature regime. Although both Forbes et al. and Vandervoort [76] show a gradual decrease in stress exponent approaching n=3 at high temperatures (1400-1500K) which is consistent with this idea, it is not yet clear whether the viscous glide contribution is significant in cases other than soft orientation single crystals where subgrain formation is suppressed due to the limited availability of slip systems.

Diffusional creep becomes the controlling mechanism at high temperatures and relatively low stresses, $\sigma/G<10^{-4}$. Creep in this regime has been classified as Nabarro-Herring or Coble creep. The flow of vacancies from grain boundaries experiencing tensile stresses to those which have compressive stresses is the origin of deformation under this mechanism. These mechanisms are characterized by a stress exponent of n=1 and a clear dependence of creep strength on grain size with large-grained materials being more creep resistant. Some recent data [77] on polycrystalline NiAl at low stress levels revealed that the stress exponent was between 1.6 and 2.1, which is also indicative of the operation of a grain boundary assisted deformation mechanism. Furthermore, there is evidence for diffusional creep processes in binary NiAl at temperatures above 1300 K and at low strain rates where grain growth during creep testing resulted in coarser grained material having higher strengths. Therefore, it can be said that diffusional creep may occur in polycrystalline NiAl at temperatures above 1200 K and at low stresses.

2.3 Ternary Alloying Effect

2.3.1 Phase Equilibria

The effect of ternary elements on the phase equilibria of NiAl+X alloys can be categorized into three groups according to the alloying element's position in the periodic table (Table 2-2) [47]. Type A elements form at least one ternary intermetallic phase with

NiAl and the solubility of these elements is usually low. Type B elements form pseudobinary eutectics with NiAl and also have limited solubility in NiAl. Finally, Type C elements display large solubilities in NiAl and often form an isostructural B2 intermetallic. The specific types of alloying behavior appear to correlate with the Group numbers in the periodic table. Type A behavior is typical of elements in Group III_B, IV_B, and V_B, Type B in VI_B, and Type C in VII_B, VIII, and III_A.

Table 2-2. Portion of periodic table illustrating the three types of NiAl-X phase equilibria [47].

IIIB	IVB	VB	VIB	VIIB	VIII			IB	IIB
Sc	Ti	V	Cr	Mn	Fe	Co	Ni	Cu	Zn
Y	Zr	Nb	Mo	Tc	Ru	Rh	Pd	Ag	Cd
La	Hf	Ta	W	Re	Os	Ir	Pt	Au	Hg

Ni-Al-X ternary phase(s)

NiAl-X pseudobinary eutectic

High solubility in NiAl and/or forms B2 aluminide

Hafnium and zirconium are classified as displaying Type A behavior. The phase diagrams of NiAl+X (where X is either Hf or Zr) in Figure 2-6 suggest that there are five intermetallic phases which can be in equilibrium with NiAl in this system, namely, Ni_3Al, Al_3Ni, NiAlX(Laves), Ni_2AlX(Heusler) and $Ni_7(X,Al)_2$ [23, 29, 78]. The occurrence of a Heusler phase and/or a Laves phase is a common feature of these ternary systems. The solubility of Hf and Zr is greater when the Ni/Al ratio exceeds unity, as shown in Figure 2-6. This suggests a solute preference for Al sites and is consistent with the structure of the Heusler phase in which Hf or Zr atoms occupy every other Al site [22]. Ternary additions may produce point defects by upsetting the Ni/Al site ratio due to strong site

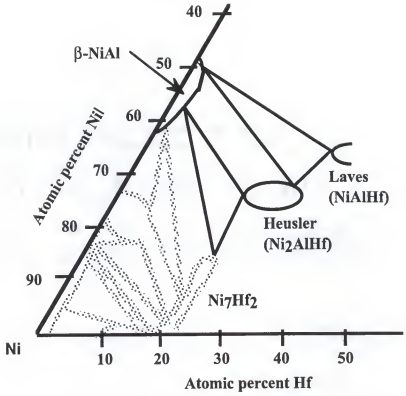

a)

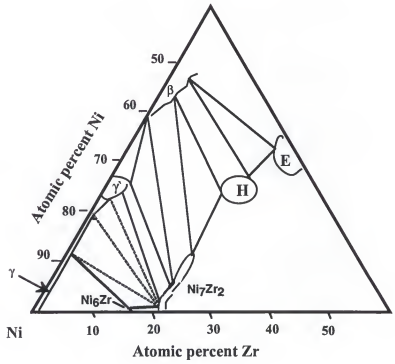

b)

Figure 2-6. (a) Ni-Al-Hf [29] and (b) Ni-Al-Zr [78] isotherms at 1300K.

preferences. The Heusler phase is essentially a further ordering of the B2 phase to Ni_2AlX, where X resides on an equivalent Al site (Figure 2-7). A strong preference for Al sites would create an effective surplus of Al-sites if %Al+%X>50, thereby increasing the number of constitutional Ni vacancies. Although silicon was not included in this classification, a Ni-Al-Si ternary isotherm in Figure 2-8 suggests that Si has a high solubility in NiAl up to 10% at 1327 K [79].

Considering the sensitivity of both the mechanical and physical properties of NiAl to stoichiometry, it would not be surprising if the Ni/Al ratio in Zr+Si-doped NiAl alloys was a critical factor in determining the phase constitution and mechanical properties of these alloys. It is believed that, in many instances, the formation of different types of phases results from variations in the kinetics of the precipitation processes, and the influence of the aforementioned defects induced by site preference, rather than shifting from one phase field to another. Previous authors [26] suggested that the G phase ($Ni_{16}X_6Si_7$, where X is either Hf or Zr) appears to be metastable at all conditions studied to date. However,an accurate Ni-Al-Zr-Si quaternary phase diagram will be needed to verify this hypothesis.

2.3.2 Microstructures

Hafnium-doped NiAl alloy

The microstructures of NiAl single crystal alloys with different levels of Hf and Si in the as-homogenized and aged conditions are summarized in Table 2-3 and the corresponding alloy compositions in Table 2-4 [25] . The homogenization treatment was 1590 K for 50 h followed by furnace cooling in alloys HS-01, 02, 06, and 07. In the case of HS-03, 04, 05, a different heating cycle (solution heat treatment of 32h at 1644 K followed by HIP for 0.5h at 1644 K, and 6h at 1255 K followed by furnace cooling) was applied.

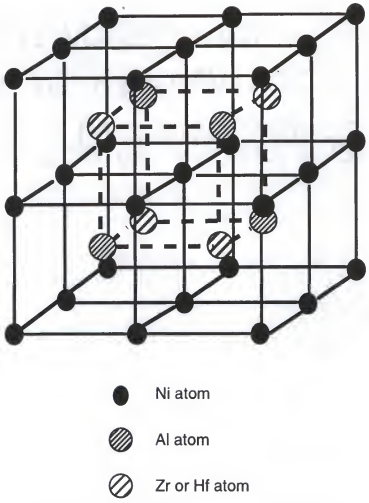

Figure 2-7. FCC structure of the Heusler phase.

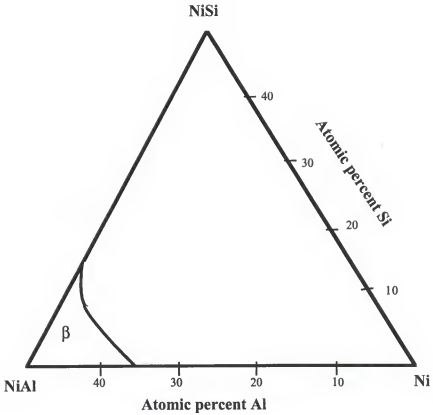

Figure 2-8. A partial Ni-Al-Si isotherm at 1300 K showing near NiAl equiatomic region [79].

Quenching experiments indicated that nucleation of the Laves NiHfSi (E phase) was aided by the presence of vacancy loops on {111} planes [80]. In addition, two morphologies of G phase were observed after cooling: (a) a high density of 10-50 nm precipitates and (b) coarser plate-like precipitates which appeared to nucleate heterogeneously. Upon furnace cooling, G-phase precipitates nucleated continuously and coarsened throughout the slow cooling period, resulting in a distribution of particle sizes.

The formation of Heusler and/or E phases at the expense of the G phase reduces the volume fraction of G phase, since the Hf originally contained in the G phase becomes tied up in the Heusler or E phase. The morphology of G phase is affected by cooling rate. Slow cooling rates (e.g. furnace cooling at 10K/min) result in platelets and cubes whereas

Table 2-3. Summary of observed microstructures. *

Alloy system (Hf / Si ratio)	As-homogenized	Short time Aging, 1h	Long time Aging, >100h	After mechanical testing at 1300K
HS-01 1.5%Hf (7.53)	Large amount of interdendritic H phase FC: G-phase; cubes and platelets			
HS-02 1 % Hf (Top: 2.6, Bottom: 3.9)	Reduced interdendritic β' phase FC: G-phase; cubes and platelets AC: G-phase; fine cubes WQ: No G-phase	1300 K homogenized+FC: H phase nucleating preferentially at G-phase platelets homogenized+AC; random nucleation of β' phase 1400 K H formation + complete dissolution of G-phase	1300 K Almost complete dissolution of G-phase, large β' phase	1200 K, 16 h H phase nucleated at G-phase plate sites and cuboids. 1300 K, 16 h H phase nucleated at G-phase plate sites. 1400 K, 16 h Coarser H phase and no G-phase
HS-03 0.5%Hf (1.17)	FC: High density of G-phase; occasional E-phase		1300 K, 100 h No significant coarsening of G-phase. E-phase coarsens significantly	
HS-04 0.5%Hf (1.66)	High density of G-phase the density of E-phase slightly higher than that of HS-03		1300 K, 100 h Both G-phase and E-phase slightly coarsened. β' phase forms adjacent to the E-phase	
HS-05 0.5%Hf (3.4)	G-phase, E-phase, H phase		1300 K, 100 h G-phase dissolved completely and slight coarsening of E-phase and H phase 1400 K, 100 h The size of E and H phase decreased 1500 K, 100 h Both E and H phase are dissolved	
HS-06 0.3%Hf (1.76)	FC: G-phase cubes and platelets and coarse E-phase AC: G-phase fine cubes		1300 K, 168 h complete dissolution of G-phase; only E-phase left	
HS-07 0.1% Hf (?)	Minimal interdendritic H FC: aligned G-phase cubes			

* from Locci et al. [25]

Table 2-4. Measured compositions of the single crystal alloys in Table 2-3. *

Alloy system	Ni	Al	Zr	Hf	Si	Hf/Si	Ni/Al	Ni/(Al+ Hf+Si)
HS-01(1.5 Hf)	48.3	49.4	0.02	1.96	0.26	7.54	0.97	0.93
HS-02(1 Hf) Top	51	47.3	----	1.23	0.47	2.62	1.078	1.04
HS-02(1 Hf) Bottom	51	47.7	----	1.01	0.26	3.88	1.069	1.04
HS-06(0.3 Hf)	49.7	49.8	----	0.3	0.17	1.76	0.998	0.99
HS-07(0.1 Hf)	50.1	49.8	----	0.1		----	1.01	1.00

faster cooling rates (air cooling) result in finer, more homogeneously distributed cuboidal particles. The G phase can be completely suppressed by rapid water quenching from the homogenization temperature. In the HS-02 alloy (Hf/Si ~3), Heusler precipitates were more stable at 1300K and coarsened at the expense of the G phase. Therefore, aging this alloy resulted in the transformation to Heusler precipitates. The microstructures of the HS-03, 04, and 05 alloys containing the same amount of Hf (0.5%) clearly shows that the Hf/Si ratio plays an important role in determining the types of phases observed. Also the stability of different phases at high temperatures is shown to be a function of Hf/Si ratio. The Heusler phase was frequently found to nucleate adjacent to the NiHfSi precipitates suggesting that their strain field may have acted as heterogeneous nucleation sites for the Heusler phase.

While the effects of Hf/Si ratio and heat treatment on the precipitation process were recognized empirically, the effect of alloy stoichiometry (Ni/Al ratio) in these alloys was not examined. Furthermore, the Si contamination during crystal growth appears to result in a loss of Al (Table 2-4). Therefore, the effect of alloy stoichiometry should be studied systematically.

The crystal structure information for the three phases of interest in the Ni-Al-Hf-Si and Ni-Al-Zr-Si systems is summarized in Table 2-5. The morphologies and orientation relationships (OR) with the β matrix are as follows:

* some alloys have no composition information due to GE's confidential policy during alloy development.

i) Heusler phase: cube-cube, polyhedrons

ii) G phase: cube-cube, fine cubes or plates

iii) E phase: $(100)_E$ // $(111)_{NiAl}$, $[010]_E$ // $[\bar{1}01]_{NiAl}$, coarse plates

The E phase forms as thin rectangular plates on {111} planes, and twelve variants are expected and typically results in the dissolution of the less-stable G phase. The kinetics of E phase formation are more sluggish due to its higher misfit and, therefore, the G phase forms initially and then transforms to E at longer times. Both phases can be distinguished easily in a $<110>_{NiAl}$ SADP (Selected area diffraction pattern).

Table 2-5. Crystallography of phases observed in Hf and Zr-doped NiAl alloy.

Phase	Lattice parameter (nm)	Structure type	Space group	#atoms/ unit cell	Reference
NiAl (β)	0.2883	CsCl	Pm3m	2	[33]
Ni_2AlHf (H)	0.6081	BiF_3	Fm3m	16	[81]
Ni_2AlZr (H)	0.6123	BiF_3	Fm3m	16	[82]
$Ni_{16}Hf_6Si_7$ (G)	1.1436	$Mn_{23}Th_6$	Pm3m	116	[83]
$Ni_{16}Zr_6Si_7$ (G)	1.1478	$Mn_{23}Th_6$	Pm3m	116	[83, 84]
NiHfSi (E)	a=0.639, b=0.382 c=0.720	Co_2Si	Pnma	12	[85]
NiZrSi (E)	a=0.647, b=0.389 c=0.726	Co_2Si	Pnma	12	[85]

Zirconium-Doped NiAl Alloy

The solubility of zirconium in NiAl is approximately 0.3% at 1300K such that, beyond 0.3% Zr, the Heusler phase tends to form. A previous study [25] showed that long term aging of the NiAl-Zr alloy at 1300 K resulted in the formation of the E-NiZrSi phase and the complete dissolution of the G-phase precipitates. However, the amount of

G-phase in a 0.05%Zr-doped NiAl (Zr/Si ratio = 0.33) alloy is more than that in the 1%Hf-doped NiAl alloy after similar heat treatments. Assuming that precipitation hardening by G phase is a major contributing factor for high temperature strength, the use of Zr instead of Hf is favored due to the higher volume fractions of G phase with the same amount of alloying. However, it is important to either (1) reduce the transformation kinetics from G to E or (2) stabilize G.

Although the high temperature strengths of the Zr-doped NiAl alloys appeared inferior to those in the Hf-doped alloys in GE's alloy screening studies, it may have been premature to abandon it. Therefore, a systematic study is needed to understand the effect of composition on microstructural evolution and the high temperature properties of Zr-doped NiAl alloys.

2.3.3 Mechanical Properties

Although several efforts including incorporating in-situ second phases with special interfaces to control crack propagation and changing the intrinsic slip behavior of NiAl have only been marginally successful for increasing the toughness of NiAl, the strength can be enhanced by such conventional methods as second phase precipitation and solid-solution hardening. Cotton et al. [47] described the possibility of defect hardening in two-phase NiAl+X systems by retaining the point defects due to the site preference of the ternary alloying element. Their results implied that it is critical to enhance the creep properties of NiAl by minimizing the defects due to alloying. Figure 2-9 shows the BDTT and 0.2% Y.S of NiAl alloys containing 2% Cr. The strength was higher when chromium was substituted for both aluminum and nickel than when it replaced only aluminum. However, the trend was reversed at high temperatures. Therefore, the point defects resulting from alloying must be considered when it comes to designing creep-resistant NiAl alloys.

Ambient Temperature Properties

The lack of a sufficient number of active slip systems to satisfy the Von Mises criterion for arbitrary plastic deformation is believed to explain the low ductility of NiAl. This motivated efforts to promote <111> slip in NiAl by alloying with ternary elements. However, no studies to date have been successful. For example, while Law and Blackburn [86] reported <111> dislocations in chromium-doped NiAl alloys and no ductility increase, Cotton et al. [47] reported that chromium additions did not activate <111> slip. In spite of this fact, Darolia et al. [10] recently reported tensile elongations approaching seven percent in <110>-oriented NiAl crystals doped with small amounts of

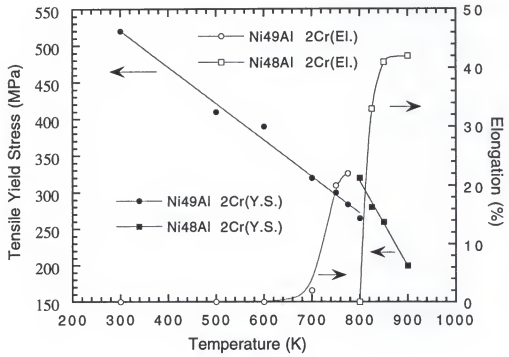

Figure 2-9. Yield stress as a function of temperature for polycrystalline NiAl alloys doped with chromium [75].

iron, gallium or molybdenum (Figure 2-10). Interestingly, the ductility passes through a maximum at small alloying additions and the benefits of doping vanish as the dopant level exceeds 0.5 percent. While it has been suggested that this effect is due to the gettering of interstitials, the real reasons for this behavior remain unknown. The effects of zirconium on NiAl has also been studied and it was found that significant strengthening occurs with only 0.1% Zr additions. However, the "BDTT" was increased to nearly twice that of NiAl [87]. Also, grain boundary strengthening by zirconium was insufficient to obtain tensile ductility leading to grain boundary cracking [43].

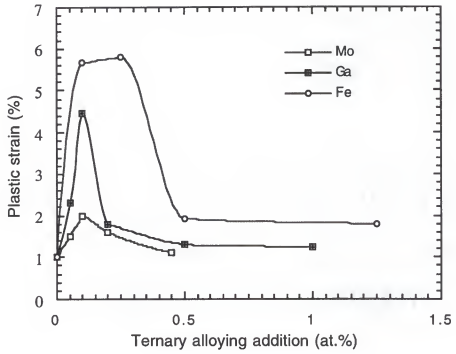

Figure 2-10. Room temperature tensile ductility of NiAl single crystals doped with iron, gallium or molybdenum tested along <110> [10].

Elevated Temperature Strength

In order to improve the creep resistance of NiAl, various strategies such as solid-solution strengthening [14], precipitate strengthening [9, 12], dispersion strengthening [16, 54] and artificial compositing [13] have been attempted. There is a decrease of about 8 orders of magnitude in the creep rate as progressive alloying additions are made from pure Ni to Ni-base superalloys [3], and the formation of a second phase is believed to be the major reason for this improvement. Similar improvements will be necessary for NiAl to compete with current superalloys.

The effects by Fe, Nb, Ta, Ti, and Zr on the creep strength of NiAl was studied by several groups [17, 21]. All of the solid solution alloys showed some improvements in strength over binary NiAl consistent with a change in stress exponent to values near 3-4. Thus, it appears that these solute additions have altered the creep process in NiAl to a viscous drag mechanism in a manner similar to that which occurs when alloying elements are added to pure metals. While solid solution hardening provides some creep strength improvements over binary NiAl, this concept is inadequate by itself and must be used in combination with other strengthening mechanisms in order to compete with superalloys.

Precipitation hardening is the most widely explored technique for improving the mechanical properties of metals. For example, the $\gamma'(Ni_3Al)$ precipitates in Ni-base superalloys are a classic example of the beneficial effect of precipitation hardening. Since Polvani et al. [12] reported enhanced high temperature strengths in two-phase NiAl+Ti alloys containing β and Heusler other elements such as Nb, Ta, Hf, Zr, and V, which form the Heusler and/or Laves phase, have been studied [88]. While these alloys are reasonably strong, the advantage diminishes when extrapolated to low stresses because of the low stress exponent (2.6~3.5). It is not clear why these alloys exhibit such low n values since most creep resistant, two-phase alloys exhibit significantly higher stress exponents than the single phase matrix. In most cases, the microstructures of the ternary alloys were probably not optimized, i.e. the second phases were too coarse. An equally

valid explanation may be that the observed values of n represent a superposition of several deformation mechanisms. By analogy to superalloys, optimizing the creep strength requires a balance between the composition and misfit of the two phases as well as the volume fraction and size and distribution of the precipitates.

Hf-doped NiAl

A comparison of the creep response of a Heusler-containing NiAl+1Hf alloy in both polycrystal and single crystal form showed different behavior. The single crystal version in <001>-oriented single crystal was not only stronger than the polycrystalline equivalent but displayed a significantly higher stress exponent, presumably because of the elimination of grain boundary deformation mechanisms [23].

In 1985, Vedula et al. [88] studied both the solid solution and precipitation hardening of NiAl alloys produced by powder metallurgy. In this study, they were the first to suggest that hafnium might be the most effective ternary alloying element for increasing the high temperature strength of NiAl. The composition of their Hf-doped alloy was Ni-53.6Al-1Hf and the increased strength was related to the Heusler precipitates.

Later, in 1991, Whittenberger et al. [17] examined the compressive creep behavior of the same Hf-doped alloys studied by Vedula, et al. However, their chemical analyses revealed that the alloy contained significant levels of iron and chromium and that it was also Al-deficient (47.0 Al) instead of Al-rich. While they also found fine Widmanstatten Heusler precipitates, their mechanical test results failed to support the advantages of hafnium in NiAl. A possible reason is that grain boundary sliding controlled the high temperature deformation where non-uniform grain sizes between samples could account for the different strength levels.

In 1993, Locci et al. [21] revisited the beneficial effect of Hf on high temperature creep strength by using 0.3 and 1% Hf-doped NiAl single crystals. The creep properties

along <001> compared favorably with the tensile creep response of NASAIR 100, a first generation single crystal superalloy (Figure 2-11). It was evident that the Hf addition contributed to the enhancement of the creep properties although it was unclear whether solid-solution strengthening or precipitation strengthening was the dominant factor. In addition, while precipitation strengthening was assumed to be the major factor, it was ambiguous as to whether Heusler or G phase was more effective. Furthermore, the formation of the Laves NiHfSi phase made the situation even more complex due to transformations between the various precipitates.

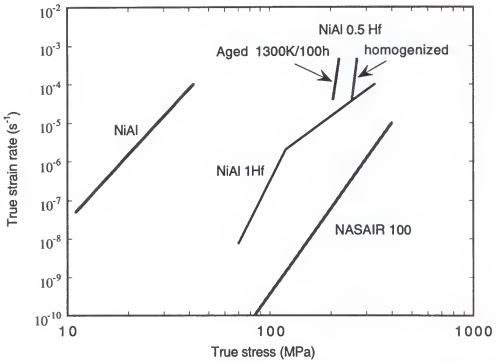

Figure 2-11. The compressive flow stress-strain rate behavior for [001]-crystals of NiAl doped with 0.5 and 1% Hf compared with binary NiAl and NASAIR 100 [21, 26].

A recent study [26] of the microstructures and mechanical properties of the Hf/Si-doped NiAl alloys attempted to clarify these issues. The creep strength of a NiAl+0.5% Hf alloy at 1300 K after homogenization treatment was better than that of samples aged

at 1300 K for 100 h. All three phases coexisted in the as-homogenized alloy whereas only the E and Heusler phases were present after aging. This result did not clearly show that the G phase is more effective than the E or Heusler phases, since dissolution of G phase was observed at 1300 K where the tests were done. However, it was anticipitated a fine, high volume fraction of G precipitates should be more effective for strengthening and this formed the impetus for the current investigation. Finally, Noebe et al. [27] examined the deformation mechanisms in single crystal alloy D176 (a trade name of one of GE's Hf doped NiAl crystal) as a function of crystal orientation and temperature and argued that solid-solution effects of hafnium included stabilizing the <110> dislocations against decomposition and reducing the ability of <100> dislocations to climb.

Zr-Doped NiAl

Smaller additions of zirconium, on the order of 0.05 atom percent, were shown to be extremely effective in strengthening NiAl at strain rates of $10^{-4}s^{-1}$ [43] while appreciably increasing the BDTT. The increase in BDTT has been attributed to the segregation of zirconium to the grain boundaries in NiAl and the subsequent inhibition of grain boundary sliding in polycrystalline NiAl [87]. Zirconium has also been shown to drastically alter the low cycle fatigue behavior of NiAl at low strain ranges [89].

Most recently, the effects of zirconium on the high temperature properties was extensively studied by Whittenberger et al [20] in the series of four powder metallurgy alloys containing 0.05, 0.1, 0.3, and 0.7 atom percent zirconium. They characterized the creep behavior of these alloys in compression between 1000 and 1400 K at strain rates ranging from 0.1 to $10^{-9}s^{-1}$. Log stress-strain curves of these alloys at 1300K indicate a slight increase in creep strength with increasing zirconium up to 0.3 atom percent (Figure 2-12).

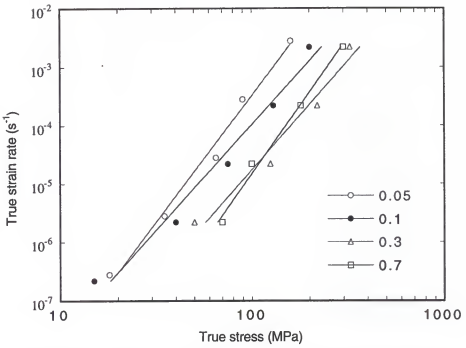

Figure 2-12. Log true stress-strain rate plot of zirconium-doped NiAl tested at 1300 K in compression [20].

2.3.4 Other Properties

It is well known that NiAl has excellent oxidation resistance and has been used as a coating for nickel-base superalloys. This resistance results from the formation of a protective alumina (Al_2O_3) scale. However, under cyclic oxidation conditions, the difference in thermal expansion coefficients between metal and oxide results in thermal stresses that lead to scale spallation. Zirconium additions (0.1 percent) significantly increase the cyclic oxidation resistance of the alloy by minimizing α-AlO_3 spalling during the cooling cycles [90].

CHAPTER 3
EXPERIMENTAL

3.1 Alloy Preparation

3.1.1 Polycrystalline Alloys

Alloys were produced from high purity elements (99.99% nickel, 99.999% aluminum, 99.95% zirconium, and 99.9999% silicon) by non-consumable arc melting under purified argon. The arc melted button size was 12.7 mm diameter x 50 mm length. A set of 8 alloys in the vicinity of equiatomic NiAl were prepared. Using the following code system all alloys were designated (Table 3-1).

Alloy Designation

1. The first letter specifies the nickel content: N indicates that the nickel content is 50% or greater and A that it is less than 50%. Z and S are abbreviations for zirconium and silicon.
2. The percent deviation from 50 % Ni is denoted by the first three digits using the formula: percent nickel x 100 (for example: 49.75 percent Ni is designated as 025). The last two digits designate the percent zirconium.

Alloys were categorized into three groups according to such factors as Zr/Si and Ni/Si ratio and solute content (Zr+Si). In Alloy Group 1, the total amount of zirconium and silicon was used as a variable with both Ni/Al and Zr/Si=1. In Group 2, the Ni/Al ratio was varied while maintaining constant zirconium and silicon concentrations

(zirconium=0.5, silicon=0.5). Finally, the Zr/Si ratio was varied in the third group of alloys while keeping the nickel concentration constant. The nominal compositions of alloys are plotted in Figure 3-1 to visualize their locations in the phase diagram.

Table 3-1. Nominal compositions of the NiAl alloys containing Zr and Si (atom%).

Alloy Group	Alloy Designation	Ni	Al	Zr	Si	Ni/Al	Zr/Si
1	AZS 01010	49.9	49.5	0.1	0.1	1	1
	AZS 02525	49.75	49.75	0.25	0.25	1	1
1 or 2	AZS 05050	49.5	49.5	0.5	0.5	1	1
2	AZS 10050	49	50	0.5	0.5	< 1	1
	NZS 00050	50	49	0.5	0.5	> 1	1
3	NZS 00030*	50	49.45	0.3	0.25	> 1	1.2
	NZ 00030*	50	49.7	0.3		> 1	∞
N.C.	NZS 10030	51	48.45	0.3	0.25		1.2

* single crystals of these target composition were grown subsequently.

3.1.2 Single Crystals

Two <001>-oriented NiAl single crystal cylinders (Ni-49.45Al-0.3Zr-0.25Si and Ni-49.7Al-0.3Zr), 25.4 mm diameter x 100 mm length, were produced via Bridgman growth from vacuum induction melting (VIM)-processed ingots. Since silicon contamination occurs when using commercial purity crucibles during crystal growth leading to the formation of G phase instead of Heusler phase, high purity alumina crucibles were used in the present study in order to minimize contamination [11]. Composition analyses were conducted at the NASA-Lewis Research Center. The

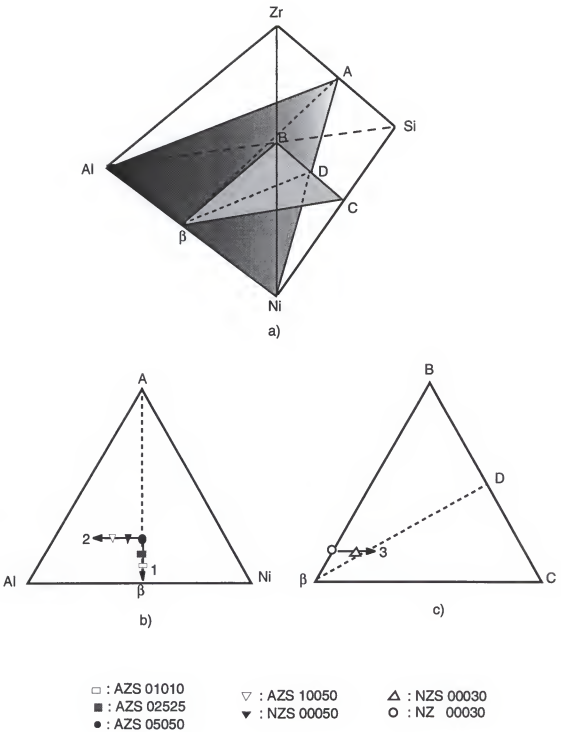

Figure 3-1 A schematic Ni-Al-Zr-Si quaternary isotherm representing the three alloy groups. In a), the plane AlNiA represents the compositions with Zr/Si=1 and plane βCB represents the compositions with 50%Ni. The alloy compositions investigated in this study lie in these composition planes as indicated in (b) and (c).

chemical composition of the NZS 00030 crystal is summarized in Table 3-2 and compared with the VIM material. The silicon content remains almost the same after crystal growth. The single crystal seed, which was pure binary NiAl and approximately 20 mm long, was cut by electro-discharge machining (EDM) from the alloy crystal prior to homogenizing in order to prevent any dilution of the alloy.

Table 3-2. Actual compositions of the starting charge material and the actual NiAl single crystal* containing Zr with or without Si (atom % or wt. ppm).

Alloy		Ni(%)	Al(%)	Zr(%)	Si(%)	C(ppm)	N(ppm)	O(ppm)
NZS 00030	VIM cast	50.29	49.11	0.31	0.25	56	5	36
	Top*	49.66	49.90	0.21	0.23			
	Bottom*	49.61	49.92	0.25	0.21			
NZ 00030	VIM cast	50.46	49.19	0.29	0.01	62	5	53

3.1.3 Orientation Measurements

The orientation of the as-grown single crystals were determined by standard Laue x-ray back reflection technique. Figure 3-2 shows a schematic diagram of Laue X-ray camera.

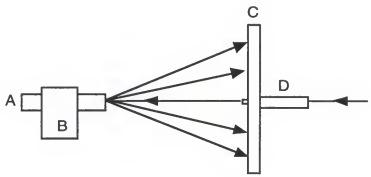

A: NiAl single crystal, B: Goniometer, C: Film holder, D: Collimator

Figure 3-2. Schematic diagram of the back-reflection Laue camera used to orient the single crystals.

3.2 Heat Treatments

GE and NASA selected 1590 K as the homogenizing temperature for their NiAl+Hf alloys based on their DTA results. In the present study, homogenizing heat treatments from 1573 K to 1673 K at 25K intervals were performed and the results indicated that 1648 K for 10 h was optimum. Thus, all homogenizing heat treatments were done using these conditions under purified argon flow. Considering the size of the single crystal, the homogenizing time was increased to 40 h from 10 h followed by furnace cooling (10 K/min). Subsequent heat treatments included reheating to, for example, 1648K followed by air cooling or water quenching as well as various aging treatments were performed in order to modify the structure accordingly. The various thermal treatments used in this study were designated as follows.

H: Homogenized, WQ: Water quenched, A: Aged, FC: Furnace cooled
AC: Air cooled

For the conveniency, the designation "H" was not included for the designation of heat treatment in the text (e.g., FC=HFC).

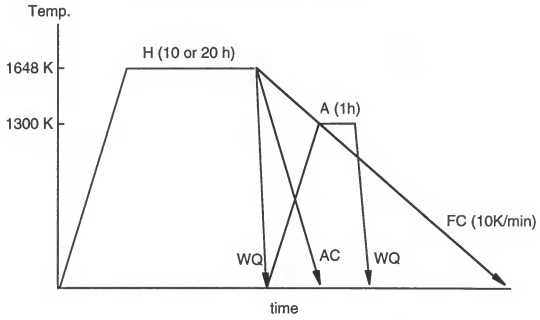

Figure 3-3. Schematic diagram of the various heat treatment schedules.

3.3 Mechanical Testing

After chemical polishing in an aqua regia solution, the crystal was oriented using the back-reflection Laue technique and EDM'd into cylindrical compression specimens parallel to the <100> axis. Specimen dimensions were 5mm diameter by 8mm in length. The specimens were chemically polished again using the aqua regia solution to remove any surface damage (recast layer) resulting from the spark cutting process. Both specimen ends in contact with the SiC platens were ground with 600 grit SiC paper using a V-block to ensure that the surfaces were parallel. After boron-nitride was sprayed on both ends as a lubricant, the samples were tested in a computerized MTS-810 servo-hydraulic system. Constant crosshead compression tests were performed under displacement control in argon at 1300K at three different strain rates:* $10^{-3}s^{-1}$, $10^{-4}s^{-1}$, and $10^{-5}s^{-1}$.

An OXY-GON Model FR 200 furnace was used to heat the sample to the desired test temperature. Argon gas was supplied by a continuos flow through a titanium-gettered furnace in order to protect both the samples and the tungsten heating element from degradation. The chamber was evacuated and back-filled with argon four times prior to heating to reduce the residual oxygen content. The actual specimen temperature was monitored with a thermocouple placed close to the specimen and temperature was maintained within ± 5K during the test. The control console allowed for both manual and automatic operation of the furnace whereby heating from room temperature to 473 K was done manually in 30 min., while from 473 K up to 1300 K heating proceeded in 45 min. as programmed. During heating, the specimen was held under a small compressive load (9 -10N) to prevent it from sliding sideways under the load control mode. This load was later added to the total applied load. Once the test temperature was reached, a 1h hold was given for the system to attain thermal equilibrium and the control mode was switched

* It is noted when testing at constant crosshead speed that the strain rate will change slightly as the specimen deforms. However, the tests were performed to small strains (~ 10 %), such that the effective strain rate was assumed to be relatively constant during the test.

from load control to stroke control.

Displacement measurements were indirectly monitored by noting the position of the crosshead during testing due to the specimen size and furnace geometry; i.e., a conventional extensometer was not used. The load displacement records were acquired digitally with appropriate data acquisition tools (Lab Tech Notebook) with buffering capabilities, as well as an X-Y plotter using the direct recording mode. From these, true stress and strain values were calculated, assuming uniform and constant-volume deformation. The compliance of the system, including the graphite rams and the SiC platens was measured at 1300 K to correct the load-displacement data (see Appendix A).

3.4 Characterization

3.4.1 Optical Microscopy

Sections from the arc cast ingots and single crystals were EDM'd for optical metallographic analysis. The samples were wet ground through 0.3 mm alumina and then either etched with saturated molybdic acid (100g MoO_3, 50ml HF, and 150 ml H_2O) or further polished on the Vibromet in order to reveal the microstructure. Differential interference contrast (DIC) was used to increase the image contrast in the Nikon Epiphot optical microscope.

3.4.2 Transmission Electron Microscopy (TEM)

Samples for transmission electron microscopy were cut from both undeformed and compression tested specimens with SiC blades on a low-speed Buehler saw. Each disk was wet ground by hand on 600 grit SiC paper to approximately 150 μm, and twin jet-electropolished in a solution of 70% ethanol, 14% distilled water, 10% butylcellusolve, 6% perchloric acid using a Struers TENUPOL-3 polishing unit (40 mA,

200 mV and 263K). TEM examinations were conducted in a JEOL 200 CX microscope operating at an accelerating voltage of 200 kV. Selected area diffraction techniques were used to identify the precipitates. In the case of smaller precipitates (<10nm), microdiffraction methods were used.

CHAPTER 4
RESULTS AND DISCUSSION

This chapter is divided into three sections. In the first section, the general microstructural evolution of the quaternary Ni-Al-Zr-Si alloy system with respect to alloy composition and heat treatment is described. Microstructure and mechanical property correlations of the single crystal NZS 00030 (Ni-49.45Al-0.3Zr-0.25Si) and NZ 00030 (Ni-49.7Al-0.3Zr) alloy are then presented in the second section in order to clarify the effect of precipitation on the high temperature strength. Included in the last section is an attempt to stabilize the G phase ($Ni_{16}Zr_6Si_7$).

4.1 Microstructural Evolution

The purpose of this section is two-fold: (1) to understand the microstructural evolution and phase equilibria with respect to Ni/Al and Zr/Si ratios and total zirconium and silicon contents and (2) to identify an alloy composition and heat treatment which would produce a desirable (stable) distribution of G precipitates with no H or E phase. Since there was essentially no concrete information about the phase diagram for the Ni-Al-Zr-Si quaternary alloy system, a set of alloys in the vicinity of the single β-NiAl phase field were produced and their microstructures were characterized accordingly.

4.1.1 Alloy Group 1

As explained in the previous chapter, Alloy Group 1 consists of three alloys: AZS 01010, 02525, and 05050. The total amount of zirconium and silicon was used as a variable while maintaining Ni/Al=1 and Zr/Si=1 in order to assess the solubility of

zirconium and silicon in NiAl. The compositions of these alloys and their relationship to the phase diagram are illustrated in Figure 3-1.

As-cast and Homogenized Structures

Optical micrographs of the AZS 01010 alloy in the as-cast (Figure 4-1(a)) and homogenized plus furnace cooled (Figure 4-1(b)) condition indicate that the interdendritic segregation was completely dissolved during homogenization with no apparent precipitation during the FC treatment. The AZS 02525 alloy, on the other hand, displayed considerably greater interdendritic segregation after casting (Figure 4-2(a)) with considerable evidence of precipitation upon furnace cooling (Figure 4-2(b)). At even higher solute levels, the AZS 05050 alloy displays higher interdendritic segregation (Figure 4-3(a)) which was not completely dissolved during homogenization (Figure 4-3(b)) indicating that this alloy is still in the two-phase field at the homogenizing temperature. Figure 4-4 shows an SEM image of the as-cast structure of the latter alloy and the bright (high Z) regions correspond to zirconium enrichment. EPMA analysis (Table 4.1) confirmed that the interdendritic regions were enriched in zirconium and silicon. The variations in the chemical compositions obtained from the interdendritic region imply that it is multi-phase instead of a specific single phase; TEM analysis of these regions (Figure 4-5(a) and (b)) revealed both H and G phases in a cube-cube relationships with the matrix.

These results indicate that the solubility limit for the sum of both zirconium and silicon (Ni/Al=1) in NiAl at room temperature appears to be greater than 0.2 percent. Considering the solubility limit of zirconium (approximately 0.3 percent at 1300 K) and silicon (up to 10 percent at 1300 K), this is not too surprising. However, if we compare this result with other work in which G-phase precipitates were observed [25], it appears somewhat ambiguous. A comparison of the chemical compositions of the two alloys (Table 4-2) suggests several possibilities. A scenario is that the different Zr/Si ratio may

Table 4.1 Compositions (at.%) of the as-cast structure of AZS 05050 alloy as analyzed by EPMA.

Area identification	No.	Ni	Al	Zr	Si
Darker region (matrix)	1	51.95	47.59	0	0.46
	2	51.53	48.06	0	0.41
	3	50.65	44.79	2.26	2.30
Brighter region (interdendritic)	1	40.67	16.68	22.70	20.55
	2	41.01	19.52	27.04	12.44
	3	46.57	23.44	21.77	8.22

* Each No. represents the average value of three neighbor spots analyzed.

Table 4-2. Nominal composition (at. %) of AZS 01010 and Locci et al's alloy [25].

Alloy	Ni	Al	Zr	Si
AZS 01010	49.9	49.9	0.1	0.1
Locci et al's alloy	49.9	49.9	0.05	0.15

shift the alloy from one phase field (i.e., β) to another phase (i.e., β+G). Although the total amount of zirconium and silicon and Ni/Al ratio are the same in two of the alloys, the ratio of Zr/Si is different; the former is 1 and the latter is 0.33. The combination of these results appears to suggest that the low Zr/Si ratio is more prone to reducing the solubility and precipitating G phase. However, this is inconsistent with speculations based upon a hypothetical phase diagram (Figure 4-5) drawn from considering higher solubility of silicon and assuming G phase is a stable and the only second phase at this composition section. If we draw a composition section of Ni-Al-Zr-Si phase diagram with a fixed Ni/Al ratio (i.e., Ni/Al=1), two of the alloys will be located on this plane. A phase

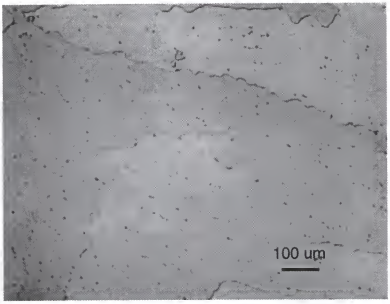

a)

b)

Figure 4-1. Optical micrographs of the (a) as-cast AZS 01010 alloy showing solute-enriched regions (black dots and lines) and (b) FC-AZS 01010 alloy.

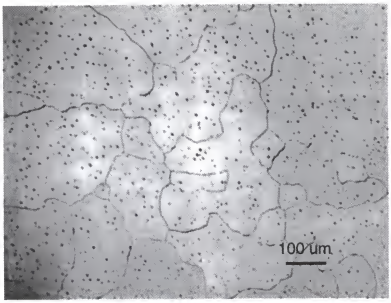

a)

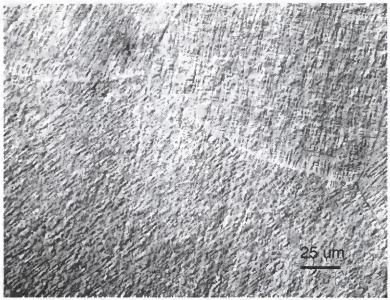

b)

Figure 4-2. Optical micrographs of the (a) as-cast AZS 02525 alloy showing solute-enriched regions (black dots and lines) and (b) FC-AZS 02525 alloy showing evidence of solid state precipitation.

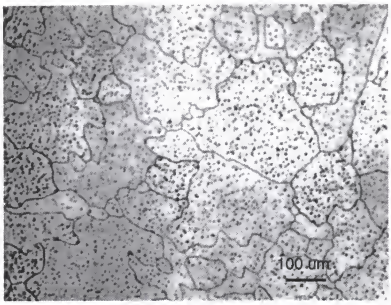

a)

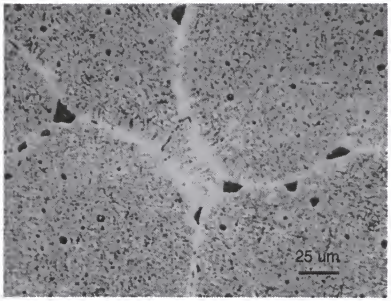

b)

Figure 4-3. Optical micrographs of the (a) as-cast AZS 05050 alloy showing solute-enriched regions and (b) FC-AZS 05050 alloy showing precipitates and undissolved solute-enriched phases (larger black dots) after homogenizing and furnace cooling (10/K).

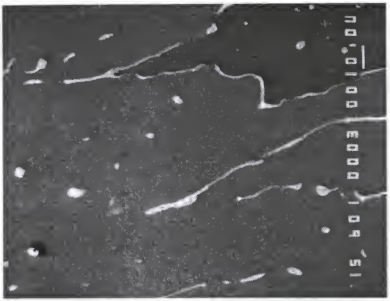

Figure 4-4. SEM image of the as-cast AZS 05050 alloy illustrating the high atomic number of the interdendritic regions.

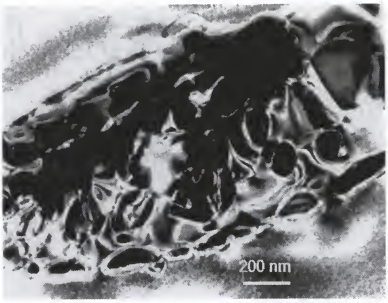

a)

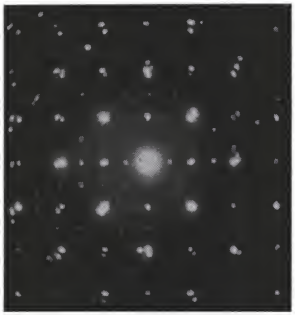

b)

Figure 4-5. (a) TEM BF image showing its multi-phase nature and (b) SADP showing extra reflection from the G and H phases from the interdendritic region of the as-cast AZS 05050 alloy.

boundary between the β phase field and β+G field will be likely line "A" in Figure 4-6.

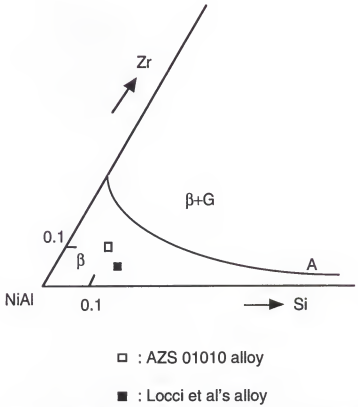

Figure 4-6. A hypothetical composition section of Ni-Al-Zr-Si phase diagram with a fixed Ni/Al ratio (Ni/Al=1) at 1300K based on the higher solubility of Si in NiAl.

This diagram suggests that an alloy with a high Zr/Si ratio will have less solubility than that with low Zr/Si ratio, i.e., our alloy should have lower solubility than the Locci, et al and, therefore, greater propensity towards precipitation. The remaining possibility is due to inaccuracies in the compositional analysis. The composition of our alloy is the nominal composition and not the result of chemical analysis, the real composition might be slightly Ni-rich considering aluminium evaporation during alloy production. Furthermore, their alloy is a single crystal grown by the Bridgman technique; in this latter case, it has been shown that variations in composition frequently exist along the length of the crystal due, for example, to aluminum evaporation during growth. Thus the chemical analysis

results may not represent the exact alloy compositions of the specimen showing the G phase; the results from several hafnium-doped NiAl single crystals strengthen this hypothesis (refer to Table 2-4 in Chapter 2).

Phase Identification

The substructural features obvious in the optical micrographs of the FC samples (figs 4-2(b) & 4-3(b))were examined in the TEM. A bimodal distribution of the G phase in the form of cuboids and plate-shaped precipitates aligned parallel to {001} planes (Figure 4-7(a)) was observed in the FC-AZS 02525 alloy. Also, coarse E precipitates were found sporadically throughout the matrix. The G phase has an f.c.c. structure (space group Fm3m) and a lattice parameter, a=1.14 nm, which is almost four times greater than that of NiAl ($4a_{NiAl}$=1.15 nm). Consequently, the G phase appears to form coherently with the NiAl matrix with a cube-on-cube orientation relationship (O.R.), i.e., $\{100\}_G//\{100\}_{NiAl}$ and $<010>_G//<010>_{NiAl}$ (See Figure 4-7(b)). On the other hand, the FC-AZS 05050 alloy developed only E-phase precipitates without any G phase. Figure 4-8(a) clearly indicates that E phase plates lie on {111} planes and the corresponding SADP is shown in Figure 4-8(b). The E phase has an orthorhombic structure with unit cell parameters, a=6.47 nm, b=3.82 nm, and c=7.26 nm (space group Pnma). Furthermore the E phase forms as thin rectangular plates on {111} planes (Fig 4-8(a)) with an O.R.(Fig 4-8(b)) given by $(100)_E//\{111\}_{NiAl}$, $[010]_E//<\bar{1}01>_{NiAl}$ [78].

From the symmetry considerations suggested by Cahn and Kalonji [91], the number of variants and morphology of the E phase precipitates can be predicted. The point group of NiAl is m3m of order 48, while that of E phase is mmm of order 4. Based on the O.R. described above, the intersection group is 2/m of order 4 (see below) Therefore, the number of predicted variants is 48/4=12. This prediction was experimentally verified by Garg et al. in their NiAl-Hf-Si alloys [80]. In addition,

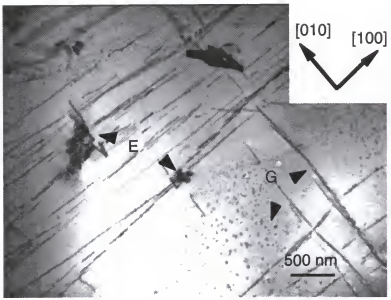

a)

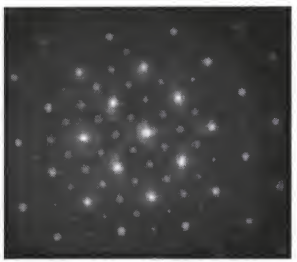

(b)

Figure 4-7. (a)TEM BF image showing bimodal G phase and coarse E phase and (b) SADP showing extra reflections from G phase in the FC-AZS 02525 alloy.

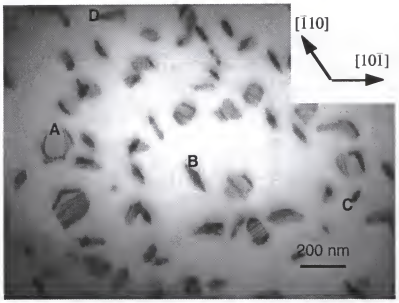

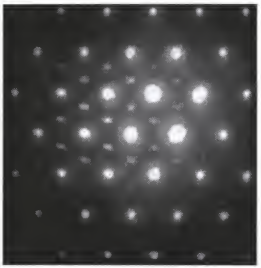

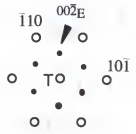

Figure 4-8. (a)TEM BF image near B=$[111]_{\beta}$ showing the E (NiZrSi) phase lying on four different $\{111\}_{NiAl}$ planes (marked A, B, C, D) and (b) SADP at [111] Z.A. showing extra reflections from E phase in the FC-AZS 05050 alloy.

$(100)_E//(111)_{NiAl}$ 4/m on $\bar{3}$

$[010]_E//[\bar{1}01]_{NiAl}$ 4/m on 2/m

$[001]_E//[\bar{1}2\bar{1}]_{NiAl}$ 4/m on 1

the pinacoid morphology of the E phase observed is consistent with the prediction from the intersection group 2/m.

The observation of different phases, i.e. G or E, in these alloys suggests that the phase field of the AZS 02525 alloy (i.e., β+G+E) may be different from that of the AZS 05050 alloy (i.e., β+E). Alternatively, the kinetics may play a role assuming that E phase is stable at both compositions i.e., the AZS 02525 alloy should have a lower driving force for transformation to E than does the AZS 05050 alloy due to the lower total solute. The microstructure of the WQA (water quenched and aged at 1300K, 1h) AZS 02525 alloy contained E phase only (Figure 4-9) consistent with this hypothesis. From this result, it was concluded that the FC-AZS 02525 alloy was not in equilibrium but that the kinetics of E phase formation was slower than in the AZS 05050 alloy due to the lower solute content implying that G phase is metastable in both alloys. Without a complete phase diagram, however, it is premature to exclude the possibility that G phase is stable at certain composition and temperature ranges in the vicinity of the NiAl single phase field.

4.1.2 Alloy Group 2

In Alloy Group 2, the Ni/Al ratio was varied while maintaining constant zirconium and silicon concentrations (zirconium=0.5, silicon=0.5). The effect of Ni/Al ratio is subtle, not only because of its influence on phase stability, but also because of the structural defects that developed (e.g., constitutional vacancies) might influence the kinetics of precipitation. The AZS 05050 (microstructure previously shown in Figure 4-3), AZS 10050 and NZS 00050 (nickel or aluminum substituted for zirconium and silicon) alloys can be classified as Group 2. The compositions of alloys in Group 2 lie along

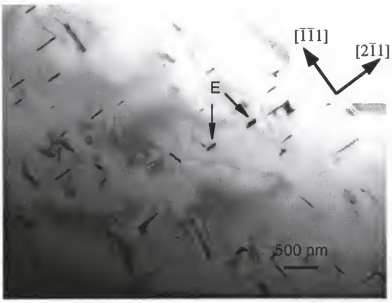

Figure 4-9. TEM BF image near B= $[011]_{\beta}$ of the WQA-AZS 02525 alloy aged at 1300K, 1h showing E phase.

arrow "2" in Figure 3-1 which is parallel to the NiAl axis.

As-Cast and Homogenized Microstructures

The as-cast and the homogenized plus furnace cooled microstructures of the NZS 00050 and AZS 10050 alloys appeared quite similar (Figures 4-10 and 4-11). As is evident, the initial segregation of both alloys was not completely eliminated suggesting that the composition still remained inside the two-phase field at the homogenizing temperature similar to the AZS 05050 alloy. A precipitate free zone (PFZ) was observed adjacent to the grain boundaries in both alloys, and its thickness appeared to depend on the alloy chemistry (i.e., Ni/Al ratio). It is well known that there are PFZ's adjacent to grain boundaries result from vacancy depletion and/or solute depletion [92]. In this case, the mechanism is unclear, although the narrower width of the PFZ in the NZS 00050 alloy compared with that in AZS 10050 alloy suggests that the former has lower diffusivity than the latter or less driving force for solute precipitation.

Also, it is noticeable that, among the three alloys, the NZS 00050 alloy (zirconium and silicon substituted for aluminum) has the lowest concentration of the interdendritic phases remaining after the homogenizing heat treatments. This result is consistent with the appearance of the β single phase field in the ternary Ni-Al-X phase diagram (where X is zirconium or hafnium) previously shown in Figure 2-3. This implies that the β single phase field always extends toward the nickel-rich side of the diagram indicating higher solubility when the alloyings element are replaced by nickel. Therefore, it is not surprising that this trend occurs even in the quaternary system.

Precipitate Identification

Only the E phase was observed in the AZS 10050 alloy (Figure 4-12(a)) while only the G phase was present (Figure 4-13(a)) in the NZS 00050 alloy. It is noted that the microstructure of both alloys is completely different from each other even though the amount of zirconium and silicon is the same. As in the case of AZS 02525 alloy, it appears that the presence of G phase is a matter of kinetics considering that point defects

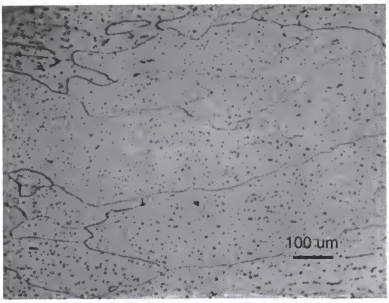

a)

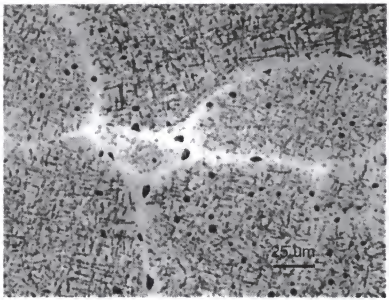

b)

Figure 4-10. Optical micrographs of the (a) as-cast AZS 10050 alloy showing solute-enriched regions and (b) FC-AZS 10050 alloy showing precipitates and undissolved interdendritic regions (black grain boundary phases) after homogenizing and furnace cooling (10/K).

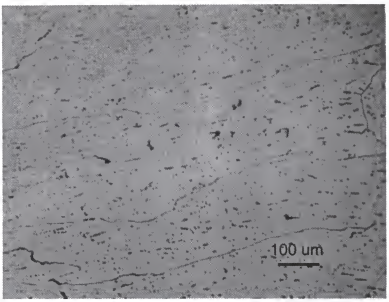

a)

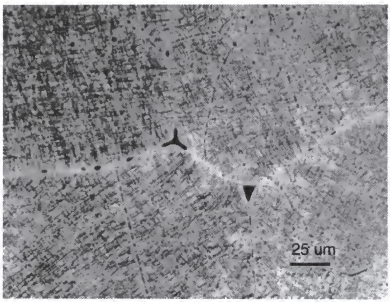

b)

Figure 4-11. Optical micrographs of the (a) as-cast NZS 00050 alloy showing solute-enriched regions and (b) FC-NZS 00050 alloy showing precipitates and undissolved interdendritic regions at grain boundaries and triple points after homogenizing and furnace cooling (10K/min).

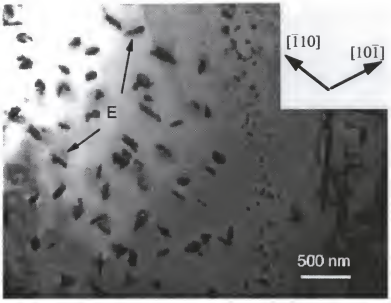

a)

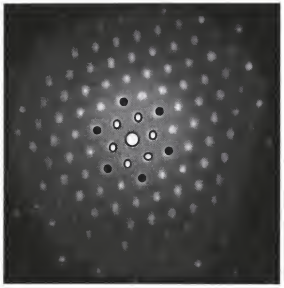

b)

Figure 4-12. (a)TEM BF image near B=[111] showing E phase and (b) <111> SADP showing extra reflections from the E phase in the FC-AZS 10050 alloy.

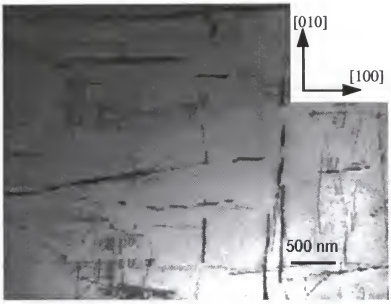

a)

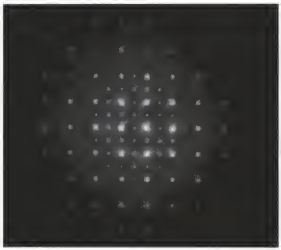

b)

Figure 4-13. (a)TEM BF image near B=[001] showing the G phase and (b) <001> SADP showing extra reflections from the G phase in the FC-NZS 00050 alloy.

resulting from site occupancy would expedite the precipitation process due to the enhancement of diffusion. In binary NiAl alloys, it is well known that the diffusivity becomes higher when the alloy composition deviates from stoichiometry. According to site occupation studies [47], zirconium and hafnium have a tendency to occupy aluminum sites whereas silicon occupies either site. Therefore, the NZS 00050 alloy (zirconium and silicon substituted for aluminium) should develop a lower number of point defects and therefore should have slower transformation kinetics from the metastable G phase to the more stable E phase. This behavior is consistent with Locci et al.'s result showing that cooling from the homogenization temperature tends to favor the nucleation of G phase with its low misfit instead of the E phase high misfit and heterogeneous nucleation mechanism [25]. On the other hand, the AZS 10050 alloy (zirconium and silicon substituted for nickel) which is expected to contain contained a larger number of constitutional defects appears to exhibit more rapid precipitation kinetics and produce the thermodynamically stable E phase in the equivalent time. This also can be an explanation that the PFZ in the AZS 05050, AZS 10050, and NZS 00050 alloys had different thicknesses in spite of similar cooling rate. Finally, this result suggests that the G phase might be stabilized further by going toward slightly higher nickel concentrations and pushes the need for determining the phase diagram in this class of material. The last section discusses this subject in greater detail.

4.1.3 Alloy Group 3

The Zr/Si ratio was varied in the third group of alloys (NZS and NZ 00030) while keeping the nickel and aluminum concentration constant. The compositions of the alloys in Group 3 lie along arrow "3" (Fig 3-(1)).

As-Cast And Homogenized Microstructures

The microstructures of these alloys before and after the homogenization treatment are shown in Figures 4-14 and 4-15. Most of the second phase is completely dissolved except some remnants at triple points and grain boundaries suggesting that the composition was still inside the two phase field at this temperature. In addition, homogenizing at higher temperatures (1673K) to reduce the remaining second phases resulted in incipient melting indicating that this particular composition did not lie in the single phase β field at any temperature; even so, since it was nearly single phase, it was possible to study the lower temperature transformations accordingly.

Precipitate Identification

Various thermal treatments were conducted on the NZS 00030 and NZ 00030 alloys in order to vary the microstructures. Water quenching from 1648 K resulted in complete suppression of any precipitation and single phase NiAl was produced in the NZS 00030 alloy. Furnace cooling (FC), on the other hand, resulted in a bimodal distribution of G phase in the form of fine cuboids and coarser plate-shaped particles aligned parallel to {001} planes (Figure 4-16(a), (b) and (c)). The G phase was easily identified from its strong reflections in the corresponding SADP (Figure 4-16(d)). The air-cooled (AC) sample contained finer (<10 nm) cuboidal G precipitates and fewer plates (Figure 4-17(a)). A precipitate-denuded zone was apparent near the platelets indicating their initial formation at higher temperatures. Furthermore, the "straightness" of the aligned plates indicates either that the dislocations which serve as the nucleation sites are edge in nature and lie on cube planes indicating that their line direction is also along <001> or more probably that elastic coherency stresses are important in the alignment process. An SADP from the latter region also clearly shows the extra reflections from the G phase. Upon aging the water quenched specimen at 1400 K for 1h (WQA), the development of coarse E phase particles occurred (Figure 4-17(b)) suggesting that the G

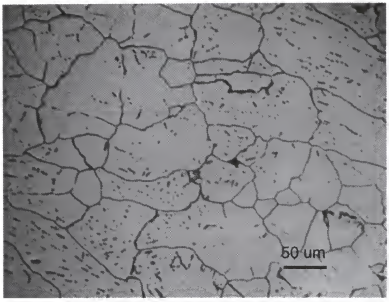

a)

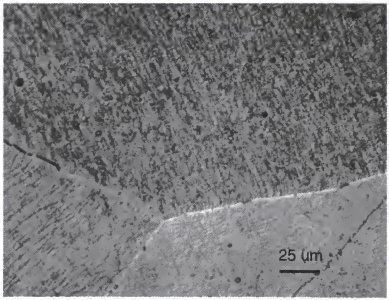

b)

Figure 4-14. Optical micrographs of the (a) as-cast NZS 00030 alloy showing solute-enriched regions and (b) FC-NZS 00030 alloy showing matrix precipitation.

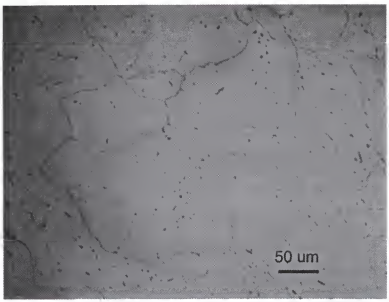

a)

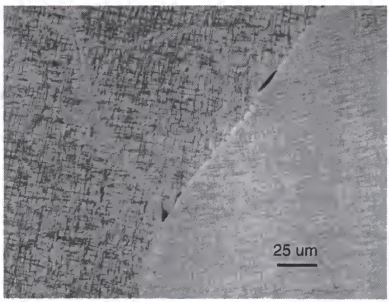

b)

Figure 4-15. Optical micrographs of the (a) as-cast NZ 00030 alloy showing solute-enriched regions and (b) FC-NZ 00030 alloy showing matrix precipitation and a small amount of undissolved interdendritic regions at the grain boundary and triple point.

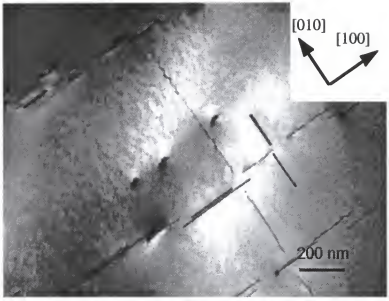

a)

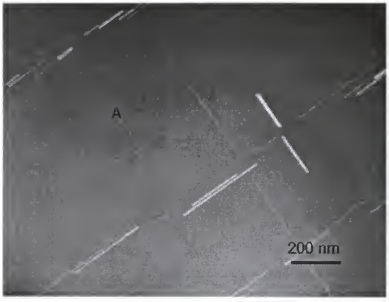

b)

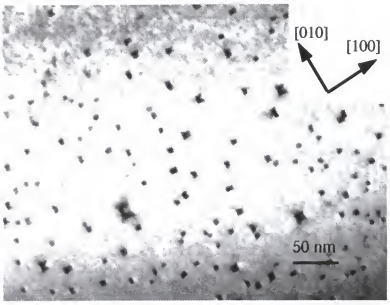

c)

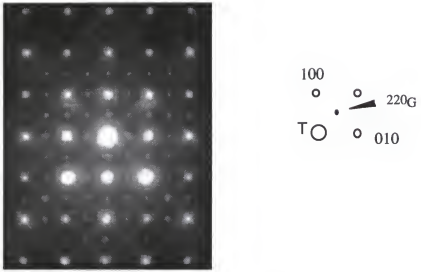

d)

Figure 4-16. TEM (a) BF, (b) DF ($g=200_G$) images near B=[001] showing plate shaped and fine cuboidal G phase, (c) Higher magnification TEM BF image of region "A" in (b), and (d) <001> SADP showing extra reflections from G phase in the FC-NZS 00030 alloy.

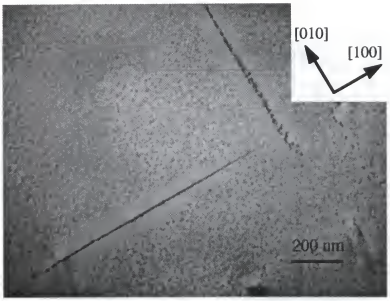

a)

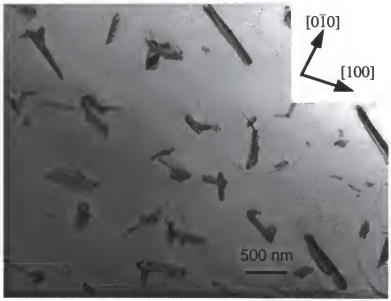

b)

Figure 4-17. TEM BF images of the (a) AC-NZS 00030 alloy showing fine G phase and denuded areas near the coarse G phase and (b) WQA-NZS 00030 alloy showing E phase.

phase observed in the furnace or air-cooled condition is metastable.

Since any silicon contamination from the arc melting process was eliminated, only Heusler phase precipitates were expected from the NZ 00030 alloy. The microstructure of this alloy after homogenization plus furnace cooling is shown in Figure 4-18(a). An SADP from this specimen (Figure 4-18(b)) shows the extra reflections of the Heusler phase near the matrix reflections consistent with a cube-on-cube O.R. with NiAl. Also it can be noticed that some of Heusler phase precipitates along <100> directions similar to the coarser plate-shaped G phase.

Homogenized and Aged Microstructure

Although the nature of G phase was revealed as metastable in the NZS 00030 alloy, the kinetics of the G to E transformation were unknown at expected service temperatures (e.g., 1300K) . Therefore, aging tests were performed on both AC and FC specimens. The alloys were aged at 1300 or 1400 K for 1h and water quenched to avoid re-precipitation during the cooling process after aging. At 1300 K, in the case of the AC specimen, the G phase appears to be relatively stable and its coarsening rate insignificant (Figure 4-19(a)). This same tendency was observed in the FC specimen (Figure 4-19(b)). Coarsening of E phase was observed at the expense of G phase in both the AC and FC specimens aged at 1400 K in (Figure 4-20(a) and (b)). The absence of E phase in both the AC and FC specimens aged at 1300K, 1h can be explained as a lack of driving force for the nucleation of this phase from the G phase which suggests that the potential G phase strengthened alloy might still be useful at this temperature range.

4.1.4 NZS 10030 alloy

Based on the evaluation of the various microstuctures indicating that G phase is more prone to form in Ni-rich compositions for given amounts of zirconium and silicon, the Ni- rich (51 percent) alloy containing the same amount of zirconium (0.3 percent) and

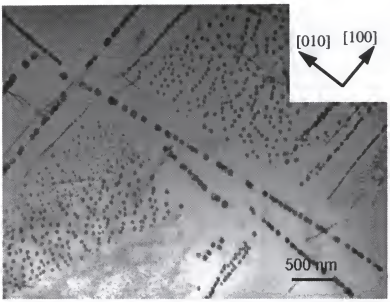

a)

b)

Figure 4-18. (a) TEM BF image near B= [001] Z.A. showing Heusler phase and (b) SADP along B= [011] Z.A. showing extra reflections from the Heusler phase in the FC-NZ 00030 alloy.

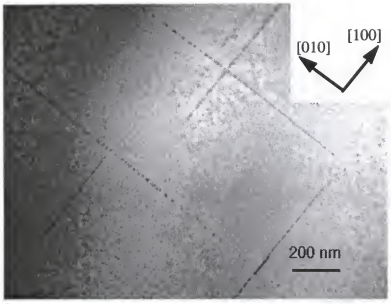

a)

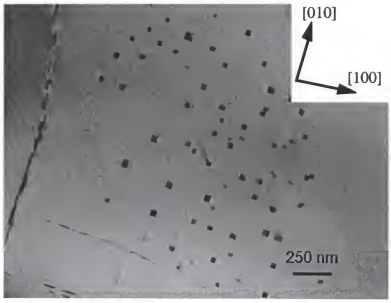

b)

Figure 4-19. TEM BF images of (a) AC-NZS 00030 alloy and (b) FC-NZS 00030 alloy aged 1h at 1300K.

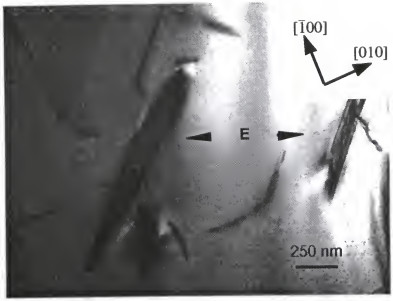

a)

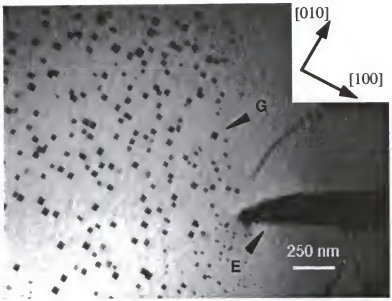

b)

Figure 4-20 TEM BF images of (a) AC-NZS 00030 alloy showing coarse E phase and (b) FC-NZS 00030 alloy, aged 1h at 1400K. Note that the G phase is being dissolved and E phase is growning in (b).

silicon (0.25 percent) that in the NZS 00030 alloy was suggested as a candidate alloy composition which might exhibit slower G to E transformation kinetics or possibly contain stable G phase.

Homogenized Microstructure

The microstructure of this alloy after homogenization and furnace cooling is shown in Figure 4-21(a). Most of the second phase was completely dissolved except for some remnants at triple points indicating that this alloy has greater solubility of zirconium and silicon than the NZS 00030 alloy.

Precipitate Identification

Water quenching from 1648 K resulted in complete suppression of any precipitation and single phase NiAl was produced. G phase precipitates were observed in the FC sample (Figure 4-21(b)) and the intensities of the extra reflections from the G phase in this alloy were also stronger than those in the NZS 00030 alloy suggesting that the volume fraction of G phase in this alloy is greater than that in the latter. The AC sample showed a much finer distribution of G phase (Figure 4-22). Finally, the WQA sample contained fine (<5nm) G phase with a few coarser cuboids (Figure 4-23), which apparently formed during aging. It was speculated that these finer particles formed during quenching due to the fact that the size of the latter was so small. Regardless of the origin of the fine precipitates, the observation of G phase in the WQA alloy aged at 1300K, 1h provides some insight for alloying schemes where the G phase might be stabilized. More experiments and discussion about G phase stability in the NZS 10030 alloy will be provided in the last section on stability.

4.1.5 Summary

Three distinct phases (G, E and H) were observed in the Ni-Al-Zr-Si quaternary system consistent with the Ni-Al-Hf-Si system depending on composition and thermal

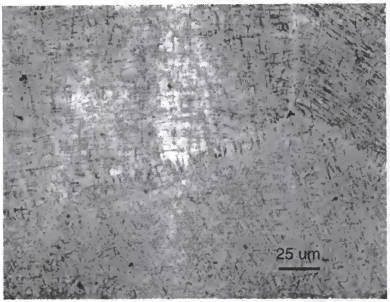

a)

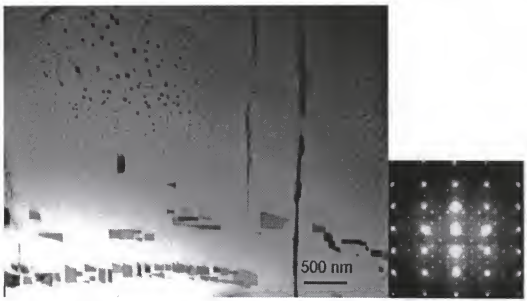

b)

Figure 4-21. (a) Optical micrograph and (b) TEM BF image close to [110] zone axis and the corresponding SADP from the FC-NZS 10030 alloy.

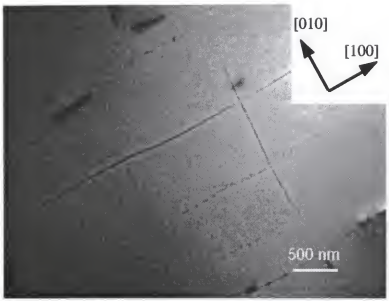

Figure 4-22. TEM BF image near B= [001] from the AC-NZS 10030 alloy.

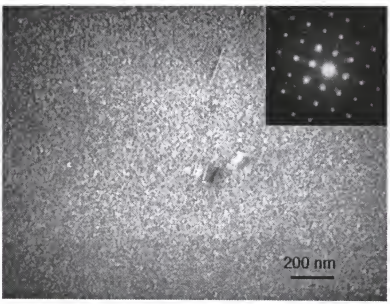

Figure 4-23. TEM DF ($g=200_G$) image near B= [001] from the WQA-NZS 10030 alloy aged at 1300K, 1h showing fine G-phase precipitate.

history. For Ni/Al and Zr/Si ratios of one, it was noted that beyond 0.5 percent solute (zirconium + silicon) contents, the alloys were in two-phase fields at the homogenizing temperature thereby limiting the potential precipitate volume fraction. However, it was observed that, for a given Zr/Si ratio, the alloys had a tendency towards increasing solubility when the Ni/Al ratio was increased. The G phase morphology was varied via heat treatment with complete suppression by water quenching. Finally, the G phase was not stable and transformed to E in all alloys except for the NZS 10030 alloy with the higher nickel concentration.

4.2 Microstructure and Mechanical Properties of NZ and NZS 00030 Single Crystals

In the previous section, the phase identification with respect to alloy composition and heat treatment was described in order to better understand the microstructural evolution of alloys in the Ni-Al-Zr-Si quaternary system. This section presents the role of microstructure on the mechanical properties, primarily the role of precipitation hardening. Based on the previous alloy screening work, NZ 00030 (Ni-49.7Al-0.3Zr) and NZS 00030 (Ni-49.45Al-0.3Zr-0.25Si) single crystals were grown parallel to <100>. Mechanical testing was then performed along the hard <001> orientations as this is better suited for structural applications and because of the desire to compare with previous studies. All tests were conducted in compression at 1300K with different strain rates ($10^{-3}s^{-1}$ to $10^{-5}s^{-1}$). Subsequent dislocation analysis were performed in order to compare the deformation mechanisms of precipitation hardened NiAl with those of binary NiAl.

4.2.1 Single Crystal Characterization

Crystal Orientation Determination

The orientations of both the NZ and NZS 00030 crystals were checked by the Laue X-ray back reflection method. Both crystals were about 5^0 off the <001> and this

was corrected prior to sectioning the ingot into compression specimens (See Figure 4-24).

As-cast and Homogenized Microstructure

The as-cast microstructure of the NZS 00030 single crystal (Figure 4-25(a)) consisted of NiAl dendrites and interdendritic zirconium-rich regions. From Figure 4-25(b), it is clear that the homogenization treatment removed almost all of the segregation although there were a few remaining micron-size particles enriched in zirconium. Also obvious in Figure 4-25(b) are striations which correspond to the G phase that formed upon furnace cooling; this is confirmed in Figure 4-26 where G phase platelets are shown. Consistent with the previous results, the AC sample contained fine G phase precipitates (Figure 4-27). The WQA sample displayed coarse particles instead of striations (Figure 4-28(a)) and these particles were identified as E-phase in the TEM (Figure 4-28(b)).

The NZ 00030 single crystal in both the as-cast and the homogenized plus furnace cooled conditions (Figure 4-29(a) and (b)) displayed similar microstructures to the NZS 00030 alloy. The initial segregation in the alloy was removed by the homogenization treatment. In this case, the Heusler phase was observed in the FC alloy (Figure 4-29(b)) indicating any silicon contamination from the crucible was negligible. The size of the H precipitates (100nm) was somewhat greater than that of the cuboidal G phase precipitates in the NZS 00030 alloy (Figure 4-29(c)). Also, it can be seen that the precipitates are aligned along the <001> direction similar to the G precipitates.

4.2.2 Mechanical Properties

Effect of Precipitate Type and Morphology on High Temperature Strength

As discussed in the previous section, the microstructures were varied by heat treatment. In order to determine the relative roles of solid-solution and precipitation hardening on strength, specimens containing either coarse E, fine cuboidal G, bimodal G,

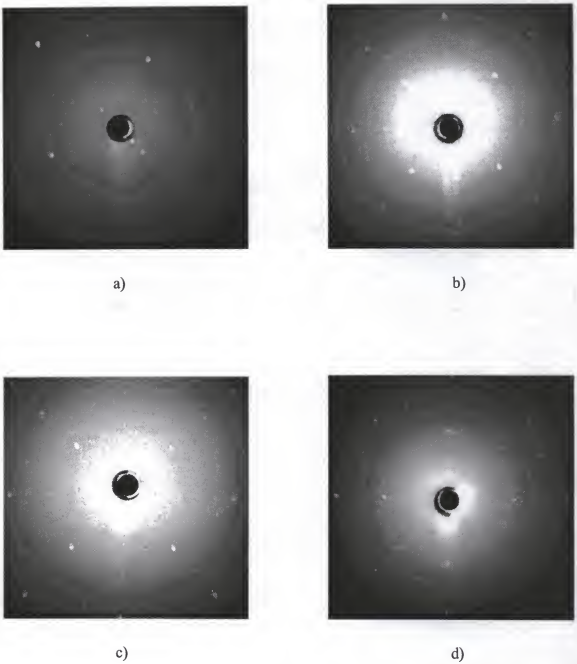

Figure 4-24. Back reflection Laue patterns of the as-grown NZS 00030 single crystal along growth direction (a) after rotation (b); as-grown NZ 00030 crystal along growth direction (c), after rotation (d).

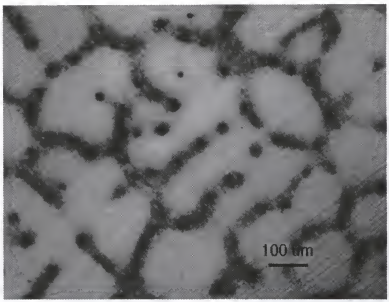

a)

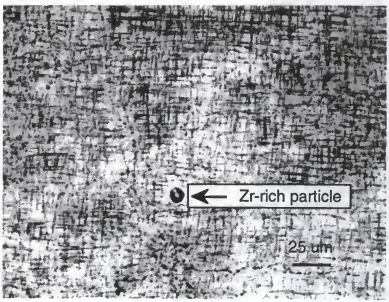

b)

Figure 4-25. Optical micrographs of the (a) as-cast NZS-00030 single crystal showing coarse dendritic structure and (b) FC-NZS 00030 single crystal containing precipitates and an undissolved Zr-rich particle after homogenizing and furnace cooling at (10K/min.).

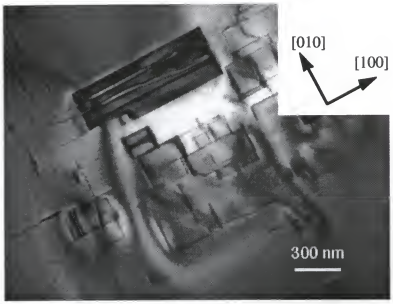

Figure 4-26. TEM BF image near B= [001] showing G plates in the FC-NZS 00030 single crystal.

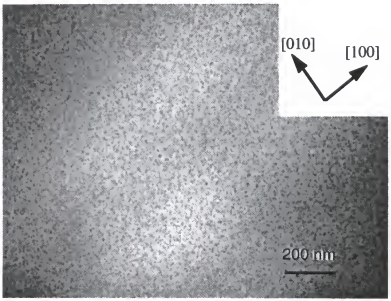

Figure 4-27. TEM BF image of the AC-NZS 00030 single crystal showing fine G-phase precipitates.

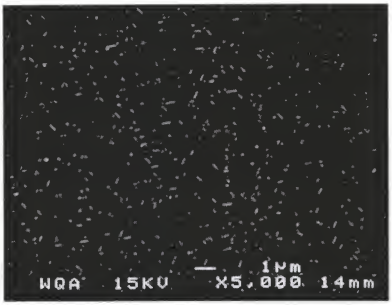

a)

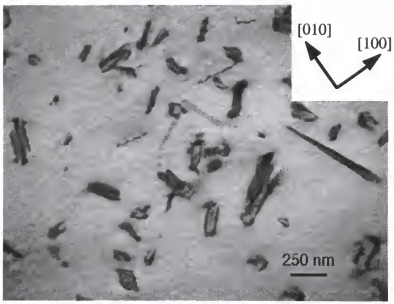

b)

Figure 4-28. (a) SEM image showing higher Zr phase (light phase) and (b) TEM BF image showing E phase from the WQA-NZS 00030 single crystal.

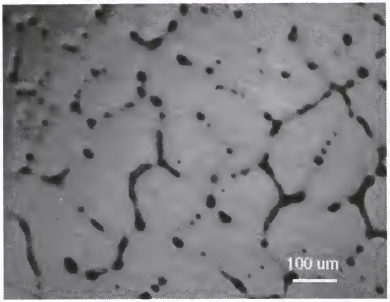

a)

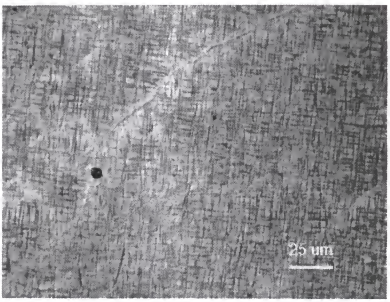

b)

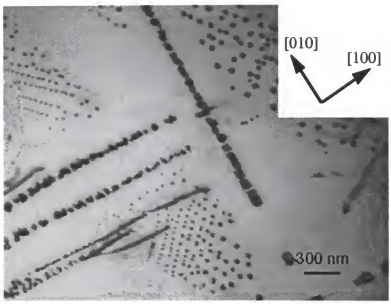

c)

Figure 4-29. Optical micrographs of the (a) as-cast NZ 00030 single crystal showing interdendritic regions, (b) FC-NZ 00030 single crystal showing matrix and an undissolved Zr-rich particle after homogenizing plus furnace cooling (10K/min), and (c) TEM BF image showing the distribution of Heusler precipitates in the FC-NZ 00030 single crystal.

H, or no precipitates were examined. In Figure 4-30, the flow behavior of each specimen is compared for a strain rate of $10^{-4}s^{-1}$. The FC-NZS 00030 crystal, which contained a bimodal distribution of G phase, exhibited a maximum in stress at approximately 3 percent strain before undergoing "flow softening". It is apparent that "flow softening" occurs suggesting an instability in the microstructure during deformation. The flow stress of the same alloy after WQA was considerably lower (approximately half) than that in the FC material and negligible flow softening occurred as expected based on the greater microstructural stability. This difference is a clear indication of the lower strengthening that results from the coarser stable E phase compared with that due to the G phase and implies that the flow softening observed in the FC specimens is due to the G to E transformation. The WQ specimen containing no precipitates initially exhibited flow softening after reaching an intermediate peak stress.

The flow softening was speculated from the precipitation and growth of the E phase during heating and testing. Since AC produced a finer distribution of G phase than FC (compare Figure 4-26 and 27), it was expected that the crystal in this condition would display the highest strength and greatest flow softening of the conditions tested. This is apparent in the true stress - true strain behavior of the AC crystal showing the highest peak strength. Finally, the flow stress of the β+H alloy (NZ 00030) was somewhat greater than that of the β+E (NZS 00030) alloy. Also, no flow softening occurred implying that this microstructure is stable as anticipated from the ternary Ni-Al-Zr diagram. Clearly, the G phase is responsible for the enhanced strength (strengths up to 350 MPa at 1300K) whereas the E phase provides little if any strengthening. Also, it appears that the Heusler phase is not as effective as G phase in our alloy {e.g., 260Mpa (G) vs. 130MPa (H), both in FC condition}. Assuming that G phase is metastable and transforms into E phase under certain conditions, a hypothetical free energy curve shown in Figure 4-31 helps explain the role of G phase. From this curve, it is evident that the matrix in metastable equilibrium with G phase will contain more solute (zirconium and

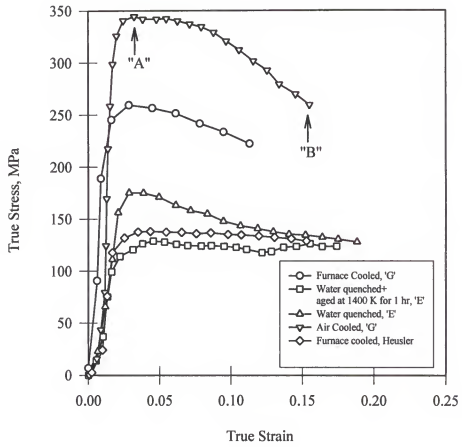

Figure 4-30. 1300K compression stress-strain curves illustrating the influence of heat treatment on the flow behavior of NZS and NZ-00030 single crystal.

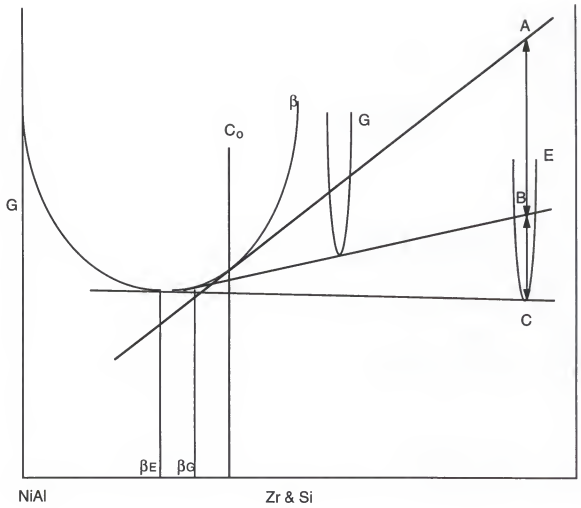

Figure 4-31. Schematic molar free energy diagram for the Ni-Al-Zr-Si system illustrating the matrix compositions equilibrated with G and E, and the reduction in the driving force for E formation by forming G initially.

silicon) in solution than that in equilibrium with the E phase. Furthermore, the formation of G will slow down the rate of E formation by reducing the driving force from "AC" to "BC". From a solid-solution strengthening point of view, therefore, a zirconium and silicon doped NiAl alloy containing G precipitates should be stronger than a comparable E phase. Also, from the precipitation strengthening point of view, it is evident that a fine and dense distribution of G phase will be more effective in strengthening than the coarse E phase.

In order to confirm the cause of the flow softening, interrupted compression tests were performed. The microstructure of the AC specimen deformed to point "A" in Figure 4-32(a) contained a sparse distribution of cube dislocations (i.e. b=<001>) in a matrix of NiAl containing the G phase. Although a small amount of E phase was observed, the effect of E on the strength was negligible at this point. However, the microstructure after deforming to point "B" (Figure 4-32(b)) contained a considerably larger amount of coarse E and less G indicating the greater stability of the latter. Significantly, the G phase in Figure 4-32(b) was similar in size to that in Figure 4-32(a) implying that the flow softening was due almost exclusively to the transformation from G to E rather than to the coarsening of G. The preferential formation of E phase at existing G phase platelets is apparent in Figure 4-33 which was taken after the 1300K deformation of the FC specimen. Whether this is related to preferential nucleation of the E phase on G or on the same dislocations that the G platelets nucleated on is unclear although it was evident that there is some correlation between these locations. Finally, the deformation substructure of both the WQ and WQA specimens in Figure 4-34 and 4-35 contain a coarse distribution of the E phase with no evidence of G. The starting microstructure of the WQ specimen was single phase NiAl supersaturated with solute and the E phase precipitated during the heating and testing cycles. Therefore, the flow stress of the WQ specimen was initially higher than that of the WQA specimen due to the solid-solution hardening; the subsequent softening is related to the solute depletion during E phase precipitation.

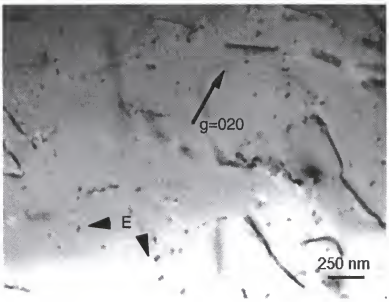

a)

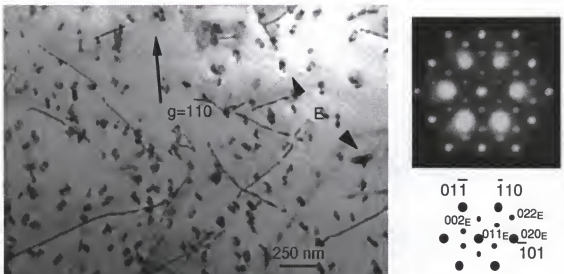

b)

Figure 4-32. TEM BF image taken near B= [001] of the AC-NZS 00030 single crystal deformed to (a) point "A" and (b) TEM BF image with the same conditions at point "B" with a micro beam electron diffraction (MBED) pattern along B= [111] indicating the presence of E phase.

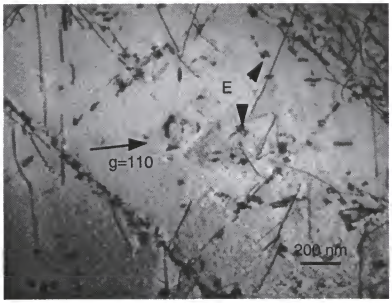

Figure 4-33. TEM BF image near B= [001] from the deformed FC-NZS 00030 single crystal.

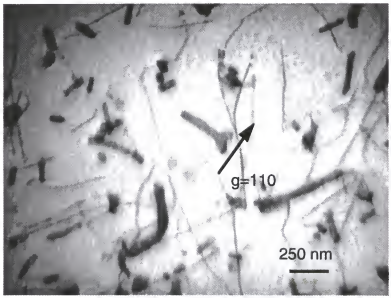

Figure 4-34. TEM BF image near B= [001] from the deformed WQA-NZS 00030 single crystal.

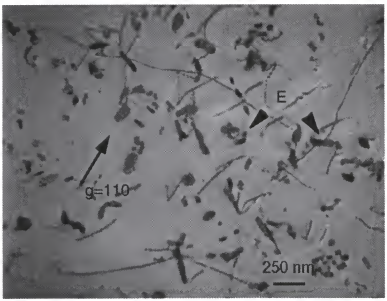

Figure 4-35. TEM BF image of the deformed as-quenched NZS 00030 single crystal.

Dislocation Analysis

Dislocation analysis was performed on the AC - NZS 00030 sample deformed to 5 (point "A") and 15 percent (point "B") to determine if there was any difference in deformation mechanism. Standard **g** • **b** analyses were conducted. Of the dislocations examined, all were determined to have <100> burgers vectors (See Appendix B). This was consistent with the results on the hafnium-doped NiAl single crystals deformed along <001> at 1300K [27] where <001> edge dislocation segments were observed almost exclusively. However, the authors claimed that the deformation mechanism in this regime occurs by a combination of <110> glide and <100> climb and explained that the temperature was high enough to cause the decomposition of <110> dislocations into two <100> segments leaving behind only indirect evidence for the operation of <110> dislocations. There was no indication that other dislocation types were activated corresponding to the flow softening, this is consistent with the G phase dissolution mechanism.

Effect of Strain Rate

The stress-strain curves for the FC-NZS 00030 crystal, which contained a bimodal distribution of G phase, at different strain rates are shown in Figure 4-36. As can be seen in these plots, the flow stress increases with increasing strain rate as expected. In addition, it is apparent that "flow softening" occurs at the strain rates $10^{-3}s^{-1}$ and $10^{-4}s^{-1}$. However, at the strain rate $10^{-5}s^{-1}$, flow softening was not observed suggesting that the total strain was too small to observe the effect or that the testing time was long enough for most of the G phase to transform to E phase prior to reaching the maximum load. The stress-strain behavior of the same alloy after water quenching and aging at different strain rates is shown in Figure 4-37. No flow softening or hardening was observed at these strain rates. This indicates that E phase is stable under mechanical stress. Figure 4-38 shows the flow behavior of the NZ 00030 single crystal containing the H phase. At a strain rate $10^{-3}s^{-1}$, slight work hardening was observed whereas at lower strain rates, a steady state

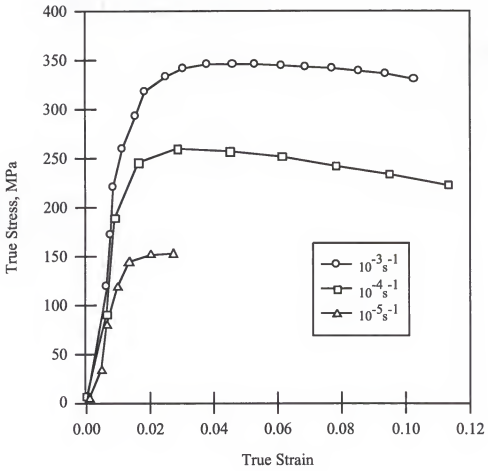

Figure 4-36. 1300K compression stress-strain curves illustrating the influence of strain rate on the flow stress of the FC-NZS 00030 single crystal containing "G" phase.

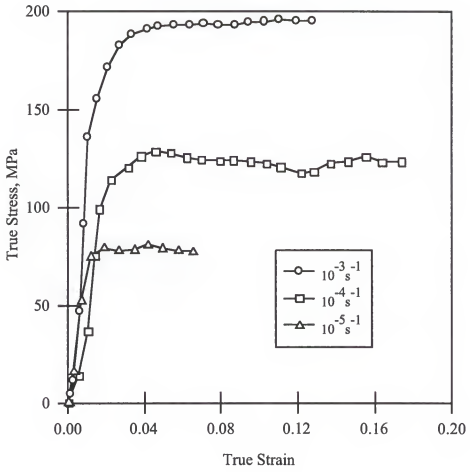

Figure 4-37. 1300K compression stress-strain curves illustrating the influence of strain rates on the flow stress of WQA-NZS 00030 single crystal containing the "E" phase. Note the lower flow stress and the negligible flow softening.

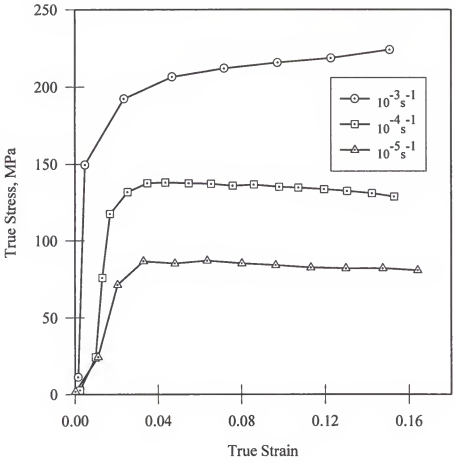

Figure 4-38. 1300K compression stress-strain curves illustrating the influence of strain rates on the flow behavior of FC-NZ 00030 single crystal.

was reached after 5 percent deformation.

The log flow stress vs. strain rate curves (Figure 4-39) were plotted to calculate the stress exponent value and to compare the creep strength of Zr/Si-doped NiAl alloys with the hafnium-doped NiAl. Steady-state stress was taken from stress-strain curves except for those cases where flow softening occurred and, in these cases, the maximum flow stress was taken. Linear regression methods were used to calculate the appropriate relationship. The deformation behavior of these crystals at 1300 K could be adequately described by the power-law relationship:

$$\dot{\varepsilon} = A\,\sigma^{n}$$

where A is a constant and n is the stress exponent, which can be calculated from the slopes of the straight lines of ln $\dot{\varepsilon}$ vs ln σ plots (Figure 4-39). Table 4-2 shows the exponent values, which are approximately 5 for all cases, from this calculation; these are in the same range as those observed for NiAl [93] and its alloys [21]. The deformation mechanism that commonly corresponds to stress exponents of 5 is dislocation climb, where n usually lies between 4 and 6 for pure metals and between 2 and 4 for alloys [94, 95] with some exceptions [96]. This classification has been shown to apply to ordered intermetallics as well [3]. While the stress exponent is not a definitive indicator of whether precipitation hardening or solid-solution hardening plays the major role in strengthening our alloys, it is clear from the TEM results and dependence of the 1300K

Table 4-2. Stress exponent values determined from the compression tests at different strain rates.

Specimen	Type of precipitate	Type of stress-strain curve	stress exponent
FC - NZS 00030	bimodal distribution of G phase	flow softening	5.7
WQA -NZS 00030	coarse E phase	steady-state	5.6
FC - NZ 00030	Heusler phase	work hardening at $1x10^{-3}s^{-1}$, steady-state at $1x10^{-4}$ and $^{-5}s^{-1}$	5

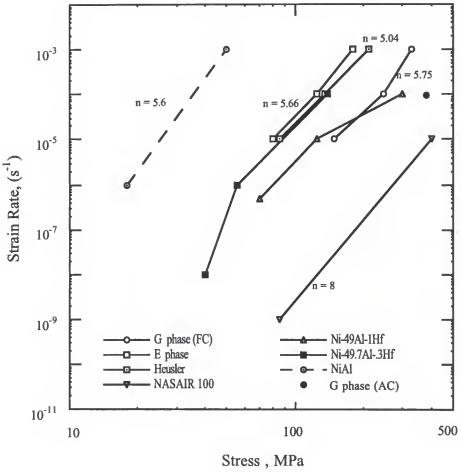

Figure 4-39. The compressive flow stress-strain rate behavior for [001]-oriented NZS and NZ 00030 single crystals compared to binary NiAl, NASAIR 100, and Hf-doped NiAl at 1300K.

behavior on mechanical properties that precipitation hardening can dominate the behavior of these alloys.

Several other things are notable from Figure 4-39. First, the creep strength of the AC specimen was comparable to that of homogenized NiAl+1Hf. Second, the lowest creep strength was observed for the WQA specimen due to the lack of any cuboidal G phase which otherwise would have contributed to the strength. Lastly, the FC specimen showed a slight deviation from the curve toward lower stress at the slowest strain rate ($10^{-5}s^{-1}$) indicating that some of the G phase transformed to E due to the longer exposure time at the test temperature.

4.2.3 Summary

The G phase provides considerable strengthening in β-NiAl but is unstable in the NZS 00030 single crystal and results in flow softening during compression testing at 1300K. Strengths at 1300K and $10^{-4}s^{-1}$ ranged from 350MPa (fine G phase) to 120 MPa (coarse E phase) with the material containing the H phase having intermediate strength. In addition, it appears that zirconium is as effective as hafnium in enhancing the creep strength in contrast to preliminary results on the zirconium-containing alloys [28]. Both at the maximum and the flow-softened stress, dislocation analysis of the AC-NZS 00030 single crystal indicate that the deformation mechanisms do not change during flow softening.

4.3 Phase stability

From the previous section it is clear that fine cuboidal G precipitates are effective in enhancing the high temperature strength of β-NiAl. However, the metastability of the G phase at the test temperature (1300K) leads to microstructural instability which degrades the strength during high temperature exposure. Consequently, it is imperative

that thisphase be stabilized before these alloys might be used in high temperature applications. Since there was no thermodynamic data available for predicting the phase equilibria in this Ni-Al-Zr-Si quaternary system, the G phase stability was empirically studied based on the previous results in both this study and the hafnium-doped NiAl studies [26]. Before the observation of G phase in the WQA-NZS 10030 alloy, it was believed that the G phase was always metastable and that its precipitation was favored by its lower misfit with the matrix. Except for the above-mentioned alloy, the other alloys which contained G phase in the FC condition developed E phase in the WQA condition seemingly confirming our speculation. In addition, assuming that hafnium and zirconium behave similarly, the Garg et al results [25, 26] appear to support the metastable nature of the G phase. In order to clarify this issue, the microstructures of the 10030 alloy were investigated in greater detail after various heat treatments. Furthermore, a geometrical approach to the phase diagram considering the chemical formula of each phase was developed in an attempt to predict the various types of precipitates observed in the Ni-Al-Zr-Si quaternary system, and to suggest ideal composition ranges which might lead to stabilization of the G phase and to increases in its volume fraction.

4.3.1 G phase Stability in the NZS 10030 Alloy

Stability at 1300 and 1400K

The AC and FC specimens were aged at 1300 and 1400 K for 1h. After aging, specimens were water quenched in order to avoid precipitation during cooling. The morphology of NZS 10030 alloy at 1300 K was clearly different from that of the NZS 00030 alloy in that coarsening of the G phase was noticeable in both the AC and FC specimens. Typically, no fine cuboidal G phase was observed in the latter (Figure 4-40 and 41). In addition, no E phase precipitates were observed after aging the AC and FC specimens at 1400 K (Figure 4-42 and 4-43). However, the G phase appears to dissolve

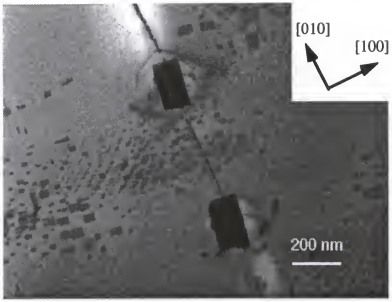

Figure 4-40. TEM BF image of AC-NZS 10030 alloy,near B= [001] aged 1h at 1300K. Note the fine and coarse cuboidal G.

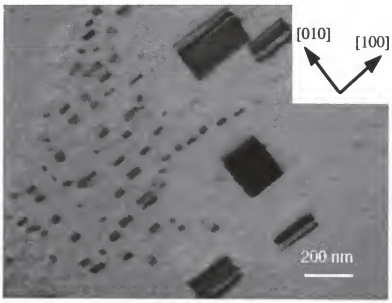

Figure 4-41. TEM BF image of the FC-NZS 10030 alloy, aged 1h at 1300K. Note the fine and coarse cuboidal G.

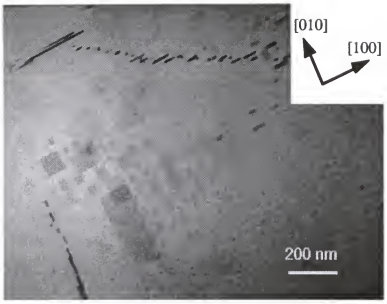

Figure 4-42. TEM BF image of AC-NZS 10030 alloy, aged 1h at 1400K. Only G precipitates were observed.

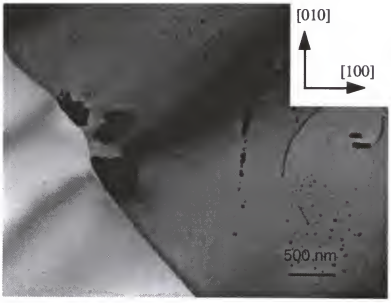

Figure 4-43. TEM BF image of a grain boundary in the FC-NZS 10030 alloy, after aging for 1h at 1400K.

at this aging temperature. Figure 4-44 shows a grain boundary precipitate which was determined to be G instead of E. It confirms that the G phase is stable a 1400K, although, its volume fraction is less than at 1300K.

The WQ specimen was aged at 1300K for 1, 16, and 100h. After aging, specimens were water quenched or furnace cooled. Fine G phase precipitates were still observed after the 16 h treatment (Figure 4-44) although their density was considerably less than in the specimens aged for 1h 1300K (see Figure 4-23) whereas the volume fraction of coarser G phase precipitates were was greater. After 100h aging and WQ, no coarse G phase were present (Figure 4-45). This indicates that 1h at 1300K was insufficient to reach equilibrium and upon quenching, the remaining solute will initiate the precipitation of fine size particles due to the decrease in solubility. After aging for 16h, less solute remained in solution and, therefore, less G phase formed upon quenching. Finally, after 100h aging, the solute concentration in the matrix was even less such that no G phase formed upon quenching.

Stability During Deformation

Since it was shown that, in the metastable alloy, the transformation from G to E was accelerated during deformation which led to flow softening, a mechanical test at 1300K was conducted on both AC and FC specimens of the stable NZS 10030 alloy, in order to determine its flow characteristics. Figure 4-46 shows the true stress-strain curve of the FC sample indicating negligible flow softening behavior. Cuboidal G precipitates were observed after deformation (Figure 4-47). Although the FC specimen showed almost steady-state flow behavior, the AC specimen showed gradual flow softening. This indicated that there was gradual dissolution of the fine G precipitates in the AC sample. It is noticeable that the strength of the AC sample was initially higher (~10MPa) and approached the same level as the FC sample. Since the microstructure of the deformed AC specimen (Figure 4-48) was similar to that of the FC specimen, it appears that

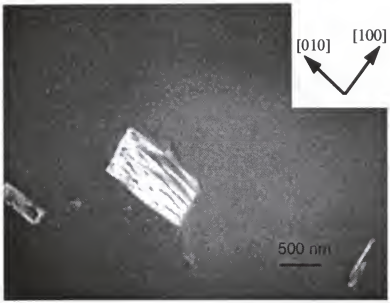

Figure 4-44. TEM DF ($g=200_G$) image of the WQA-NZS 10030 alloy, aged 16h at 1300K.

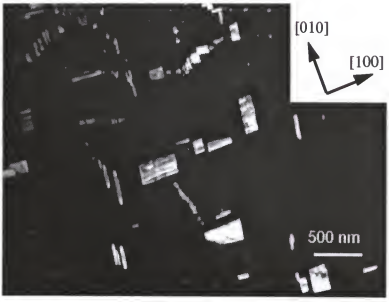

Figure 4-45. TEM DF ($g=200_G$) image of the WQA-NZS 10030 alloy aged 100h at 1300K.

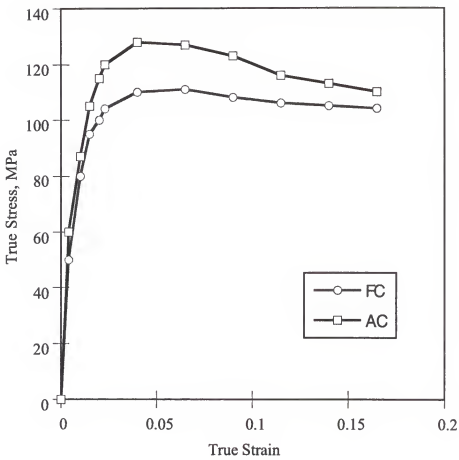

Figure 4-46. 1300K compression stress-strain curves at $10^{-4}s^{-1}$ strain rate illustrating the influence of heat treatment on the flow stress of the NZS 10030 alloy.

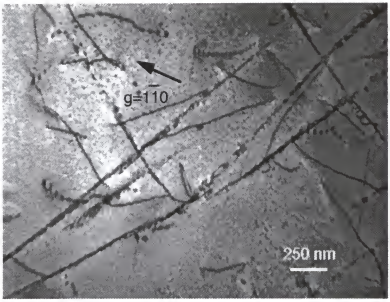

Figure 4-47. TEM BF image of the AC-NZS 10030 alloy after deforming ~15 % at 1300K.

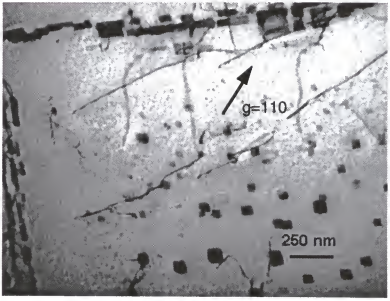

Figure 4-48. TEM BF image of the FC-NZS 10030 alloy after deforming ~15%, at 1300K.

increasing the Ni content in the Zr/Si-doped NiAl alloy have offsetting effects; i.e., it tends to stabilize the G phase while decreasing its volume fraction due to the higher solubity. This leads to the relatively low strength of the stabilized alloy with the low volume fraction of "stable" G. Therefore, alloying to increase the volume fraction of stable G remains a challenge. Another noteworthy point is that this solubility increase in Ni-rich Ni-Al-Zr-Si alloys might explain the ambiguous results regarding the effect of G phase precipitates on the Hf-doped NiAl single crystals [21]. Specifically, the authors suggested that the strength of air or furnace cooled specimens were the same, even though the microstructures were completely different. The air cooled sample contained very fine cuboidal G phase precipitates whereas the furnace cooled sample contained a bimodal distribution of G phase similar to ours. The present results indicate that the fine cuboidal G phase observed in both the FC and AC specimens probably formed during the cooling stage otherwise it would significantly affect the strength.

4.3.2 A Geometrical Approach on the Phase Diagram Considering Chemical Formula

Since there are no Ni-Al-Zr-Si or Ni-Al-Hf-Si quaternary phase diagrams available, it was not possible to determine whether G is a stable or metastable phase under the conditions (composition and temperature) studied. Except for the NZS 10030 alloy, it appears that G is metastable in both our alloys and in the hafnium-doped alloys studied elsewhere [25, 26]. Thus, it was of interest to use this information to predict what direction to take in order to identify other compositions that might develop large volume fractions of stable G phase. The approach taken was based on geometrical considerations involving the chemical formulae for the various phases.

General Concept

In order to visualize this construction, a schematic Ni-Al-Zr ternary phase diagram is drawn in Figure 4-49. At fixed temperature and pressure, the Gibbs phase rule

predicts a maximum of four phases in equilibrium in any portion of the phase diagram. regions of three-phase equilibria form triangles in isothermal sections of the ternary

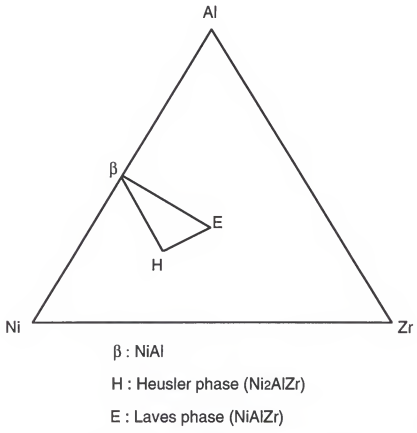

Figure 4-49. A simplified Ni-Al-Zr phase diagram.

phase diagram. The phases at the corners of a given triangle form single-phase fields and are bounded by two-phase tie lines. For simplicity, the ternary diagrams have been drawn without showing the homogeneity range of each single-phase or two-phase region, i.e., each single-phase region is represented by a point and each two-phase region by a line on the diagram. One of the advantages of this simplified phase diagram is its ability to apply at any temperature below the solvus temperature. An alloying scheme can be drawn from this diagram. For example, if we decide to make a two-phase alloy (β+H), then the line "βH" should give a clue as to how much and which element should be added.

In reality, what it means is if we want to design a NiAl alloy hardened by Heusler (Ni_2AlZr) precipitates, simply following the tie line "βH" from β to H in the phase diagram will direct the selection of the alloy composition. It indicates that zirconium atoms gradually replace aluminum atoms while holding the nickel content constant. This alloying scheme will minimize the possibility of the alloy containing unwanted phases. Also, if we want NiAl containing E, then the line "βE" will provide some direction as to how to obtain such an alloy. In this case, both nickel and aluminum atoms should be replaced by zirconium (i.e. Ni/Al=1). Thus, for systems which do not have a phase diagram, this concept can be used to provide some guidance for alloy design in the ternary system.

Application to a Real System (Ni-Al-Fe)

In order to determine whether this geometrical consideration is applicable to any ternary system, the Ni-Al-Fe phase diagram (Figure 4-50) was selected. The rationale behind the choice was its complexity since, near β_2 two other phases {$\lambda(Ni_2Al)$, $\theta(FeAl_3)$} exist as well as two ternary phases {Al_9FeNi (τ_1) and $Al_{10}Fe_3Ni$ (τ_2)}; if the approach works in this system, it was assumed that it might work in other systems also. Point "A" (τ_2) was calculated based on its chemical formula and the arrow "β_2 A" was drawn. Starting on the β_2 side this arrow intersects the following phase fields: $\beta_2 \rightarrow \beta_2 + \lambda \rightarrow \beta_2 + \lambda + \tau_2 \rightarrow \beta_2 + \tau_2 \rightarrow \tau_2$. This result appears to be inconsistent with a prediction from the geometrical approach which is supposed to be $\beta_2 \rightarrow \beta_2 + \tau_2 \rightarrow \tau_2$. However, this complexity originated from the existence of just one extra single phase, λ. Assuming that no other single phase exists, then λ can be replaced to β_2 which is the closest chemical formula among the three phases β_2, τ_1, and τ_2. The intersecting phase field can be reduced down to $\beta_2 \rightarrow \beta_2 + \tau_2 \rightarrow \tau_2$, which is consistent with the prediction.

Table 4-3. The chemical compositions in wt. % converted from at.%.

Chemical formula	Ni	Al	Fe
$Al_{10}Fe_3Ni$ (τ_2)	12	54	34
NiAl (β_2)	68	32	

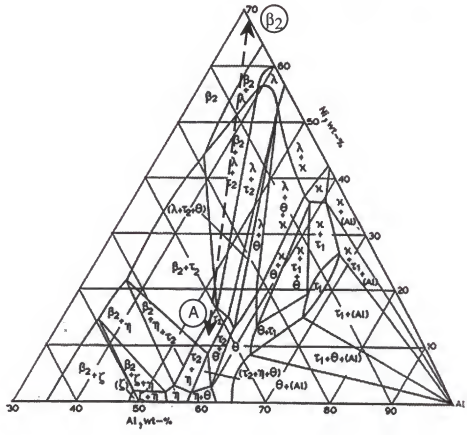

Figure 4-50. Ni-Al-Fe isotherm at 1173K [97].

Application to the Quaternary Ni-Al-Zr-Si System

Now, we can extend this concept to the quaternary phase diagram which is not easy to visualize due to the 3-D nature of the isotherm. Figure 4-51 shows a simplified Ni-Al-Zr-Si tetrahedral isotherm containing β, Heusler, G, and E phase. For simplicity, it will be assumed that the triangle NiAlX drawn for Zr/Si =1 contains both the E and G phases (G actually lies slightly below this triangle). Here, each point represents a single-phase region and each line, a two-phase region, each triangle, a three-phase field, and each

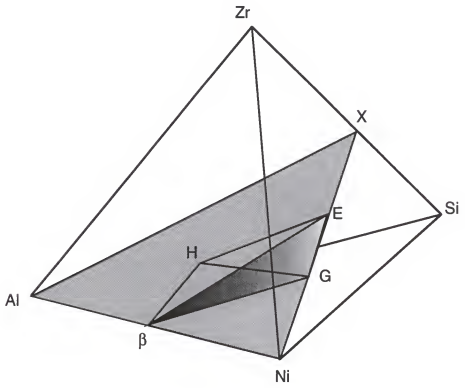

β : NiAl

H : Heusler phase (Ni_2AlZr)

E : Laves phase (NiZrSi)

G : G phase ($Ni_{16}Zr_6Si_7$)

Figure 4-51. A simplified Ni-Al-Zr-Si phase diagram.

tetrahedron, a four-phase field. The same principle can be applied as described above for the ternary systems. Specifically, the line βG provides a direction that might favor the formation of the G phase, namely that aluminum atoms should be replaced by zirconium, silicon, and also nickel in a specific ratio.

It should be recalled that this diagram does not consider the homogeneity ranges of the various phases. In reality, the NZS 00030 alloy (Ni-49.45Al-0.3Zr-0.25Si) will be located inside of the βHGE tetrahedron, which is a four-phase field. However, the stable phase observed in this alloy was E phase indicating that the real phase diagram has a much larger β+E two-phase field. Also, the NZS 10030 alloy (Ni-48.45Al-0.3Zr-0.25Si) containing stable G phase is located outside the βHGE tetrahedron near line βG. Considering that the β+G two-phase field should have some range of homogeneity, this is also possible. Even though this approach may not predict the exact phase equilibria needed to design an alloy, it can be useful in providing guidance in selecting alloying additions and/or changes. While more quantitative information is needed in order to identify the exact compositions for producing stable β+G structures, it is possible to estimate what direction to take by considering the NiAlX triangle shown in Figure 4-52.

Since the Zr/Si ratio in most of our alloys is approximately 1, it is reasonable to assume our alloys are located on this triangle. In order to calculate the linear relationship of the line βG in terms of Ni, Al, and X component, a triangle βNiYwas drawn (Figure 4-52). We can draw two equations out of this; one is β +Y +Ni = 50 and the other is 43YG = 7NiG where YG is Ni content-50. If we assume the composition of G phase is $Ni_{16}Zr_7Si_7$, point G will be at 57 Ni. From these relationships, any alloy composition lying in line βG can be calculated once the Ni composition is fixed. For example, if the Ni content is 51% (designated as point "A" in the line βG), the other compositions will be determined automatically. The portion of Ni in the triangle βNiY will be the extra Ni (YG component) which is 1=51-50, then the portion of Y content will be (43/7)x1=6.14 and Al = 42.86. Also, we can convert Y into Zr and Si which, since Zr/Si =1, gives Zr=3.07

and Si=3.07. From this calculation the alloy containing 51Ni-42.86Al-3.07Zr-3.07Si should contain β+G only. The line βE can be calculated using the same method. Consider a triangle ZNiE, the ratio of Zβ to βE is 16.7/50 (because XE/ENi=AlZ/ZNi, and

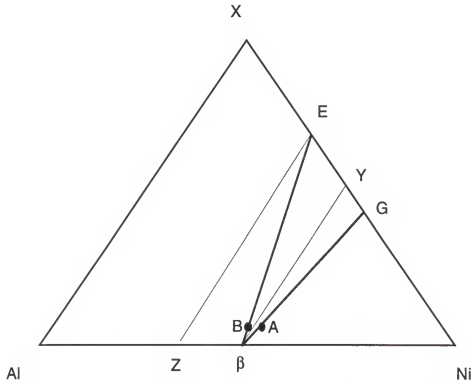

Figure 4-52. A portion of the quaternary isotherm taken from Figure 4-51.

Ni+Al+X = 100, 2XE = ENi

points β and Y are at the centers of lines NiAl and NiX, respectively.

AlZ=33.3 , therefore, Zβ=16.7). The chemical composition following this line can be calculated. For example, suppose Ni is 49 (designated as point "B" in the line βE), then the extra Ni in the triangle ZNiE will be 15.7=49-33.3. The Al content can be calculated from the above relationship as, Al=15.7*50/16.7=47. Finally the X content, which is the sum of Zr and Si, will be 100-(49+47)=4. Since Zr/Si=1, then Zr=2 and Si=2. The chemical compositions which will lie along lines βG and βE are calculated in Table 4-4.

The results of these calculations are summarized in Table 4-5 and plotted in Figure 4-53. Combining these results and the calculated figure, an interesting result is obtained. Significantly, the alloys AZS 05050 and 10050, in which the E phase is stable, are located to the left of line βE indicating a lower probability of producing G phase. If we consider the homogeneity ranges, of only the single phase fields, it is presumed that these alloys lie in the two-phase E + β field. Secondly, NZS 10030 alloy, which appears to contain

Table 4-4. Calculated composition lying along the line βG or βE.

type of line	predicted phases	Ni	Al	Zr	Si
βG	G + β	51	42.86	3.7	3.7
	G + β	50.5	46.5	1.5	1.5
βE	E + β	49	47	2	2
	E + β	49.5	48.5	1	1

Table 4-5. Phases observed in the Zr/Si-doped NiAl alloys.

	FC	Aged	WQA
AZS 01010	No ppt		
AZS 02525	G phase		E phase
AZS 05050	E phase		
AZS 10050	E phase		
NZS 00050	G phase	G and E phase	E phase
NZS 00030	G phase		E phase
NZS 10030	G phase	G phase	G phase
*0.5Hf-NiAl	G phase	G and E phase	

* Garg et al's results from an alloy with Hf/Si=1.17 ratio [26].

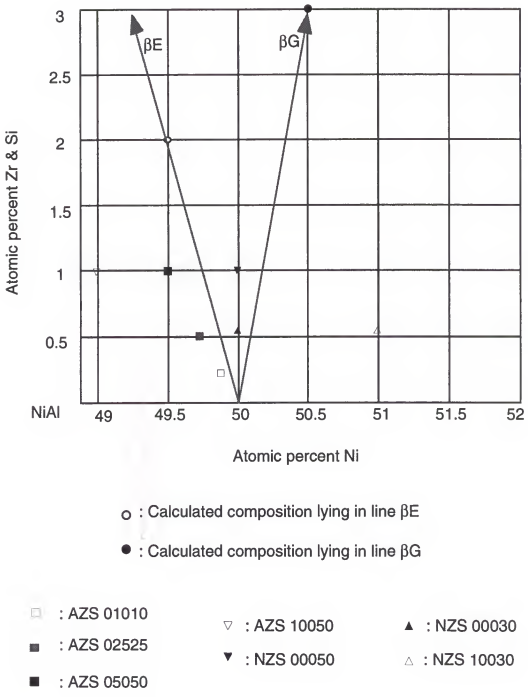

Figure 4-53. A schematic section from the NiAl side of the Ni-Al-Zr-Si system, illustrating the location of the experimental alloys with respect to the βE and the βG lines (see text) along with two alloys calculated to fall on these lines.

stable G phase,is located on the right side of line βG suggesting that this alloy maybe in the β+ G two phase field . Lastly, AZS 02525 and NZS 00030 alloys are located near or inside three-phase β+ G+E field. These alloys displayed G phase upon furnace cooling, although, the stable E phase formed after water quenching and aging. We suggest a scenario where these compositions are in the E + β phase field but where,the G phase precipitates initially due to its low misfit as was discussed in previous sections.

While this geometric approach is oversimplified and does not include any thermodynamic calculations, our experimental results and the results on the Hf-doped NiAl alloys, whose composition is similar to our NZS 00050 alloy, were all fairly consistent with this diagram. Furthermore, this diagram was used to predict the composition range where we might obtain stable G phase, and the preliminary studies on alloy NZS 10030 seem to confirm this.

4.3.3 Summary

The G phase observations from the WQA-NZS 10030 alloy proved that G phase can be a stable phase in these alloys. A phase map drawn using simple geometric considerations was used to correlate guidelines for predicting the alloying behavior of alloys in this system. Furthermore, this map was able to direct the alloy composition where we can obtain higher volume fractions of stable G phase excluding other second phases. However, further work is needed to verify or disprove this approach empirically.

CHAPTER 5
SUMMARY

Three distinct phases (G, E and Heusler) were observed in the Ni-Al-Zr-Si quaternary system, consistent with the Ni-Al-Hf-Si system, depending upon alloy chemistry and heat treatment. At ratios of Ni/Al=1 and Zr/Si=1 and beyond 0.5 percent total solute (zirconium + silicon), the alloys could not be completely homogenized at 1648K; this, of course, limits the maximum volume fraction of precipitate that can be achieved at lower temperature. It was observed that, for a given Zr/Si ratio, the alloy has a tendency towards increasing solubility with increasing Ni/Al ratio. Both fine cuboidal and coarser plate-shaped G formed depending on cooling rate. Furthermore, G precipitation appeared to be completely suppressed by water quenching from the homogenizing temperatures in all of the alloys studied. Finally, G phase was observed to be metastable in all cases except the higher nickel NZS 10030 alloy which had a low volume fraction of stable G phase.

The high temperature strengths at 1300K and $10^{-4}s^{-1}$ ranged from 350 MPa (fine G phase) to 120 MPa (coarse E phase) with the Heusler-containing material having intermediate strength. Precipitation hardening from fine cuboidal G precipitates was identified as the major factor in enhancing high temperature strength in the alloys studied. It was also shown that zirconium appears to be as effective as hafnium in enhancing the creep strength of NiAl. Unfortunately, the metastability of the G phase leads to flow softening in the NZS 00030 single crystal deformed at 1300 K, thereby limiting the beneficial effects of the G phase on properties. Dislocation analyses performed after different levels of strain (softening) indicate that <100> dislocations are dominant and

that no other deformation mechanism contributed to the flow softening. The stress exponents of the single crystals studied were nearly 5 which is typical for NiAl single crystals under similar testing conditions.

The observations from the WQA-NZS 10030 alloy proved that G phase is stable at certain composition ranges and temperatures. However, the fine precipitates observed appear to form upon cooling. This phenomenon may explain some ambiguities in the G stability and the mechanical test results in the GE/NASA studies on Hf-containing alloys; i.e. why their precipitates appeared to be more stable, and why the flow stress of both furnace and air cooled specimens were the same even though the microstructures were significantly different. Since their alloy may be Ni rich due to Al evaporation during crystal growth, the composition may have been close to our NZS 10030 alloy (Ni-rich). A phase map drawn using simple geometrical considerations was developed in order to aid the empirical efforts to produce alloys containing a fine distribution of stable G phase.

APPENDIX A
CALCULATION OF TRUE STRESS AND STRAIN CONSIDERING MACHINE COMPLIANCE

The engineering stress and strain can be expressed as following equations (1) and (2), also true stress and strain, (3) and (4)

$$\text{Engineering stress: } s = \frac{P}{A_0} \quad (1)$$

$$\text{Engineering strain: } e = \frac{l_0 - l}{l_0} \quad (2)$$

$$\text{True stress: } \sigma = \frac{P}{A} \quad (3)$$

$$\text{True strain: } \varepsilon = \ln\frac{l_0}{l} \quad (4)$$

where P is the applied load, A_0 the initial cross-section area, l_0 and l the initial and the final specimen heights. The final specimen height is obtained by subtracting the displacement of the system from the total displacement (Figure A-1). The true stress and strain are calculated from the engineering stress and strain by equation (5) and (6).

$$\text{True stress: } \sigma = s(1 - e) \quad (5)$$

$$\text{True strain: } \varepsilon = \ln\frac{l}{l - e} \quad (6)$$

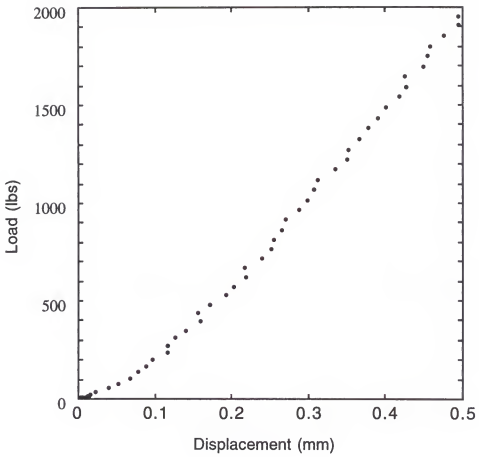

Figure A-1. Load-displacement plot for the system at 1300K.

APPENDIX B
DISLOCATION ANALYSIS

A typical dislocation analysis of NiAl consists of imaging dislocations and determining which diffracting conditions produce little, if any contrast. The micrographs below show an area of dislocations at different **g** vectors. At $\mathbf{g} \cdot \mathbf{b} = 0$, the dislocation is invisible. From the cross product of these **g** vectors it is evident that b=100 burgers vector is dominant.

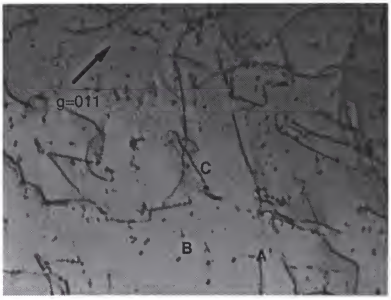

Figure B-1. Dislocation analysis for the AC-NZS 00030 single crystal after deforming to point "A" in Figure 4-30 taken near B= [011] zone axis.

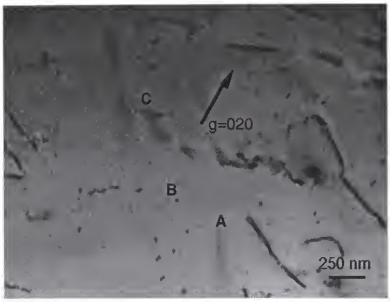

a)

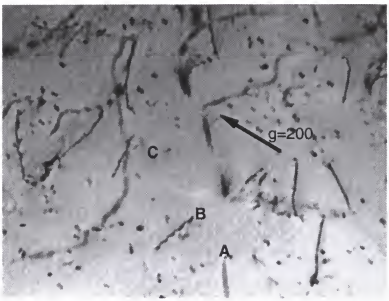

b)

Figure B-2. Dislocation analysis for the AC-NZS 00030 single crystal after deforming to point "A" in Figure 4-30 taken near B= [001] zone axis.

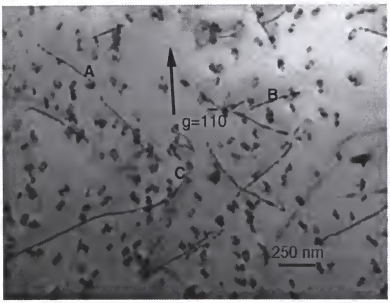

a)

b)

c)

Figure B-3. Dislocation analysis for the AC-NZS 00030 single crystal taken at point "B" in Figure 4-30 close to [001] zone axis.

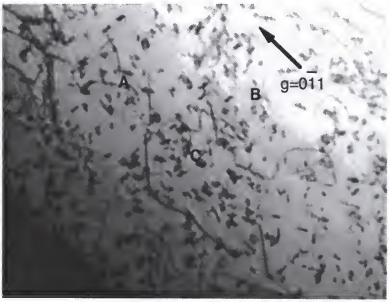

Figure B-4. Dislocation analysis for the AC-NZS 00030 single crystal taken at point "B" in Figure 4-30 close to [011] zone axis.

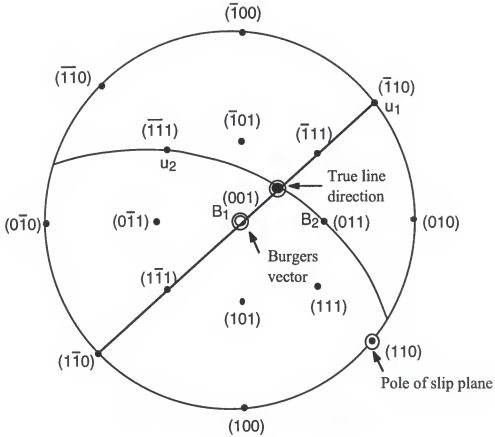

Figure B-5. Stereographic projection showing trace analysis of a dislocation in AC-NZS 00030 single crystal deformed at 1300K.

REFERENCES

1. Pratt and Whitney Aircraft, *The Aircraft Gas Turbine Engine and Its Operation*, United Technologies Corp., Pratt and Whitney Group, 1960.

2. Sims, C. T. and Hagel, W. C., *The Superalloys*, 1972, John Wiley & Sons, New York.

3. Sims, C. T., Stoloff, N. S., and Hagel, W. C., *Superalloys II*, 1987, John Wiley & Sons, New York.

4. Buckman, R. W., Jr. and Goodspeed, R. C., *Refractory Metal Alloys*, 1968, Plenum, New York.

5. Lund, R. W. and Nix, W. D., Acta Metall., 1976, **24**, p. 469-481.

6. Larsen, D. C. et al., *Ceramic Materials for Advanced Heat Engines*, 1985, Noyes, Park Ridge, NJ.

7. Miracle, D. B, Acta Metall., 1993, **41**, p. 649-684.

8. Noebe, R. D., Bowman, R. R., and Nathal, M. V., *Physical and Mechanical Metallurgy of NiAl*, 1994, NASA Technical Report.

9. Darolia, R., .J. of Metal, 1991, **43**, p. 44-49.

10. Darolia, R., Lahrman, D., and Field, R., Scripta Metall., 1992, **26**, p. 1007-1012.

11. Levit, V. I. , Bul, I. A. , Hu, J. and Kaufman, M. J., Scripta Metall., **34**, 1996, p. 1925-1930.

12. Polvani, R. S., Tzeng, W. S., and Strutt, P. R., Metall. Trans. A, 1976, **7A**, p. 33-40.

13. Walter, J. L. and Cline, H. E., Metall. Trans. A, 1973, **4A**, p. 33-38.

14. Whittenberger, J. D., J. Mat. Sci., 1988, **23**, p. 235-240.

15. Whittenberger, J. D., Westfall, L. J., and Nathal, M. V., Scripta Metall., 1989, **23**, p. 2127-2130.

16. Whittenberger, J. D., Ray, R., Jha, S. C., and Draper, S., Materials Science and Engineering A, 1991, **138**, p. 83-93.

17. Whittenberger, J. D., Nathal, M. V., Raj, S. V., and Pathare, V. M., Materials Letters, 1991, **11**, p. 267-272.

18. Whittenberger, J. D., Ray, R., and Jha, S. C., Mat. Sci. Eng., 1992, **A151**, p. 137-146.

19. Whittenberger, J. D. and Luton, M. J., J. Mat. Res., 1992, **7**, p. 2724-2732.

20. Whittenberger, J. D. and Noebe, R. D., Metall. Trans. A, 1996, **27A**, p. 2628-2641.

21. Locci, I. E., Dickerson, R., Bowman, R., Whittenberger, J. D., Nathal, M. V., and Darolia, R., *High Temperature Ordered Intermetallic Alloys V*, MRS Symp. Proc., 1993, **288**, p. 686-692.

22. Markiv, V. Ya. , Voroshilov, Yu. V., Kripyakevich, P. I., and Cherkashin, Yu. V., Soviet Physics-Crystallography, 1965, **9**, p. 619-620.

23. Kumar, K. S., International Materials Reviews, 1990, **35**, p. 293-327.

24. Locci, I. E., Noebe, R. D., Bowman, R., Miner, R. V., Nathal, M. V., and Darolia, R., *High Temperature Ordered Intermetallic Alloys IV,* MRS symp. Proc., 1991, **213**, p. 1013-1018.

25. Locci, I. E. , Dickerson, R. M. , Garg, A. , Noebe, R. D. , Nathal, M. V. and Darloia, R., J. Mater. Res., 1996, **11**, p. 3024-3038.

26. Garg, A., Noebe, R. D. and Darolia, R., *Characterization of the Microstructure of a Hf-doped NiAl Sinlge Crystal Alloy Containing Different Levels of Si Contaminant,* To be published.

27. Noebe, R. D., *Deformation Behavior of the Single Crystal NiAl Alloy D176*, 1995, NASA.

28. Walston, W. S. and Darolia, R., *High Temperature Ordered Intermetallic Alloys V*, MRS symp. Proc., 1994, **288**, p. 1221-1229.

29. Nash, P., West, D. R. F., Metal Science, 1981, **15**, p. 347-352.

30. Hughes, T., Lautenschlager, E. P., Cohen, J. B., and Brittain, J. O., J. Applied Physics, 1971, **42**, p. 3705-3716.

31. Westbrook, J. H., J. Electro. Soc., 1956, **103**, p. 54-63.

32. Westbrook, J. H., *Mechanical Properties of Intermetallic Compounds*, 1959, John Wiley & Sons, New York.

33. Taylor, A. and Doyle, N. J., J. Appl. Cryst., 1972, **5**, p. 201-209.

34. Bradly, A. J. and Taylor, A., Pro. Roy. Soc., A, 1936, **159**, p. 56-72.

35. Wasilewski, R. J., J. Phys. Chem. Sol., 1968, **29**, p. 51-56.

36. Wasilewski, R. J., J. Phys. Chem. Sol., 1968, **29**, p. 39-49.

37. Georgopoulos, P. and Cohen, J. B., Acta Metall., 1981, **29**, p. 1535-1551.

38. Chang, Y. A. and Neuman, J. P., Prog. Sol. St. Chem., 1982, **14**, p. 221-301.

39. Hahn, K. H. and Vedula, K., Scripta Metall., 1989, **23**, p. 94-97.

40. Lautenschlager, E. P., Kiewit, D. A., Brittain, J. O., Trans. Metall. Soc. AIME, 1965, **233**, p. 1297-1302.

41. Jacobi, H. , Vassos, B. and Engell, H. J., J. Phys. Chem. Sol., 1969, **30**, p. 1261-1271.

42. Yamaguchi, Y., Aoki, T., and Brittain, J. O., J. Phys. Chem. Sol., 1970, **51**, p. 1325-1343.

43. Bowman, R. R., Noebe, R. D., Raj, S. V., and Locci, I. E., Metall. Trans. A, 1992, **23A**, p. 1493-1507.

44. Fu, C. L. and Zou, J., *High Temperature Ordered Intermetallic Alloys VI,* MRS Symp. Proc., 1995, **364**, p. 91-96.

45. Hosoda, H., Inoue, and Mishima, Y., *High Temperature Ordered Intermetallic Alloys VI,* MRS Symp. Proc, 1995, **364**, p. 437-442.

46. Kao, C. R. , Pike, L. M., Chen, S. L. and Chang, Y. A., Intermetallics, 1994, **2**, p. 235-247.

47. Cotton, J. D., Noebe, R. D., and Kaufman, M. J., *Internation Symposium on Structural Intermetallics*, Darolia, R., Lewandowski, J. J., and Liu, C. T. Edit., TMS, Warrendale, PA. 1993, p. 513-522.

48. Duncan, A. J., *Site Occupation and Mechanical Properties of Iron-Doped NiAl*, Ph.D. Dissertation, 1995, University of Florida.

49. Anderson, I. M., Duncan, A. J., and Bentley, J., *High Temperature Ordered Intermetallic Alloys VI,* MRS Symp. Proc, 1995, **364**, p. 443-448.

50. Wynblatt, P., Acta Metall., 1967, **15**, p. 1453-1460.

51. Vogl, G. and Sepiol, B., Acta Metall., 1994, **42**, p. 3175-3181.

52. Hancock, G. F. and McDonnell, B. R., Phys. Stat. Sol. (a), 1971, **4**, p. 143-150.

53. Kao, C. R. and Chang, Y. A., Intermetallics, 1993, **1**, p. 237-250.

54. Whittenberger, J. D., Gaydosh, D. J., Kumar, K. S., J. Mater. Sci., 1990, **25**, p. 2771-2776.

55. Forbes, K. R., *Mechanisms of High Temperature Deformation of NiAl Single Crystals*, Ph. D. Dissertation, 1994, Stanford University.

56. Shankar, S. and Seigle, L. L., Metall. Trans. A, 1978, **9A**, p. 1467-1476.

57. Ball, A., and Smallman, R. E., Acta Metall., 1966, **14**, p. 1517-1526.

58. Ball, A., and Smallman, R. E., Acta Metall., 1966, **14**, p. 1349-1355.

59. Wasilewski, R. J., Butler, S. R., and Hanlon, J. E., Trans. Met. Soc. AIME, 1967, **239**, p. 1357-1364.

60. Field, R. D. , Lahrman, D. F. and Darolia, R., Acta Metall., 1991, **39**, p. 2961-2969.

61. Mills, M. and Miracle, D. B., Acta Metall., 1993, **41**, p. 85-95.

62. Cotton, J. D., Noebe, R. D., and Kaufman, M. J., Intermetallics, 1993, **1**, p. 3-20.

63. Lloyd, C. H. and Loretto, M. H., Phy. Sta. Solidi., 1970, **39**, p. 163-170.

64. Dollar, M., Dymek, S., Hwang, S. J., and Nash, P., Scripta Met., 1992, **26**, p. 29-34.

65. Baker, I. and Schulson, E. M., Metall. Trans. A, 1984, **15A**, p. 1129-1136.

66. Miracle, D. B., Acta Met., 1991, **39**, p. 1457-1468.

67. Pascoe, R. T. and Newey, C. W. A., Met. Sci. J., 1968, **2**, p. 138-143.

68. Kim, J. T. and Gibala, R. *High Temperature Ordered Intermetallic Alloys IV*, 1991, MRS Symp. Proc. **213**, p. 261-266

69. Bowman, R. R. , Noebe, R. D., and Darolia, R., *Mechanical Properties and Deformation Mechanisms of NiAl*, 1989, NASA.

70. Bowman, R. R., Noebe, R. D., Raj, S. V., and Locci, I. E., Metallurgical Transactions A, **23A**, 1992, p. 1493-1507.

71. Takasugi, T., Kishino and Hanada, S., Acta Metall., 1993, **41**, p. 1009-1020.

72. Lutze-Birk, A. and Jacobi, H., Scripta Met., 1975, **9**, p. 761-765.

73. Berkowitz, A. E., Jaumot, F. E. Jr., and Nix, F. C., Phys. Rev., 1954, **95**(5), p. 1185-1189.

74. Soiman, M.S. and Mohamed, F. A., Mat. Sci. Eng., 1982, **55**, p. 111-119.

75. Mohamed, F.A and Langdon, T. G., Acta. Metall., 1974, **22**, p. 779-788.

76. Vandervoort, R. R. Mukherjee, A. K. and Dorn, J. E., Trans. ASM, 1966, **59**, p. 930-944.

77. Raj. S. V. and Farmer, S. C., *High Temperature Ordered Intermetallic Alloys V*, 1993, MRS Symp. Proc. **288**, p. 647-652.

78. Markiv, V. Ya, Matushevskaya, N. F., Rozum, S. N., and Kuz'ma, Yu. B., Izv. Aka. Nauk SSSR, Neo. Mat., 1966, **2**, p. 1356-1359.

79. Guard, R. W. and Smith, E. A., J. Inst. Met., 1959, **88**, p. 369-370.

80. Garg, A. , Noebe, R. D.and Darolia, R., Acta Metall., 1996, **44**, p. 2809.

81. Lee, K. J. and Nash, P., J. Phase Equilibria, 1991, **12**(1), p. 94.

82. Nash, P. and Pan, Y. Y., J. Phase Equilibria, 1991, **12**(1), p. 105.

83. Gladyshevskii, E. I., Dopov. Akad. Nauk. Ukr. RSR, 1962, **4**, p. 481-483.

84. Spiegel, F. X. , Bardos, D., and Beck, P. A., Transaction of the Metallurgical Society of AIME, 1963, **227**, p. 575-579.

85. Villars, P. and Calvert, L. D., *Pearson's Handbook of Crystallographic Data for Intermetallic Phases*. 1985, Metals Park, OH., ASM.

86. Law, C. C. and Blackburn, M. J., *Rapidly Solidified Lightweight Durable Disk Material*, 1985, United Technologies Corp., Pratt and Whitney Group.

87. Noebe, R. D., Behbehani, M. K., Scripta Met., 1992, **27**, p. 1795-1800.

88. Vedula, K., *High Temperature Ordered Intermetallic Alloys*, MRS Symp. Proc., 1985, **39**, p. 411-421.

89. Noebe, R. D. , Lerch, B. A. , and Rao, K. B., *High Temperature Ordered Intermetallic Alloys VI,* MRS Symp. Proc, 1995, **364**, p. 291-296.

90. Barrett, C. A., Oxidation of Metals, 1988, **30**, p. 361-390.

91. Cahn, J. W. and Kalonji, G., *International Conference on Solid-Solid Phase Transformations*., TMS-AIME, 1982, p. 3-14.

92. Starke, E., Jr., J. of Metals, 1970, 22, p. 54-63.

93. Forbes, K. R., Glatzel, U., Darolia, R., and Nix, W. D.,. Metall. Trans. A, 1995, **27A**, p. 1229-1240.

94. Garofalo, F., *Fundamentals of Creep and Creep-Rupture in Metals*, M.E. Fine, Weertman, J., and Weertman, J. R. edit., 1965, Macmillan, New York.

95. Mukherjee, A. K., Bird, J. E., and Dorn, J. E., Trans. of ASM, 1969, **62**, p. 155-179.

96. Sherby, O. D. and Burke, P. M., Prog. Mat. Sci., 1966, **13**(7), p. 325-390.

97. Bradley, A. J. and Taylor, A., J. Inst. Met., 1940, **66**(2), p. 53-65.

BIOGRAPHICAL SKETCH

Yongjin Lim was born on October 22, 1959, in Taejon, Korea. He attended Taejon High School from which he graduated in 1978. He received the B.S degree at the Yonsei University at Seoul, in 1982, where he majored in metallurgical engineering. He entered Yonsei Graduate School where he earned his Master of Engineering in 1984. After serving in the army for 6 months, he worked for the Korea Institute of Energy and Resource until 1986. In 1987, he shifted his career to the Agency for Defense Development and was involved in the projects of rocket motorcase development and tank armor plate design for 5 years. In 1992, he entered the University of Florida for a Ph.D program in order to develop an academic career. He completed his Ph.D at the University of Florida in 1997. He has two sons and a dedicated wife.

I certify that I have read this study and that in my opinion it conforms to acceptable standards of scholarly presentation and is fully adequate, in scope and quality, as a dissertation for the degree of Doctor of Philosophy.

Michael J. Kaufman, Chairman
Professor of Materials Science and Engineering

I certify that I have read this study and that in my opinion it conforms to acceptable standards of scholarly presentation and is fully adequate, in scope and quality, as a dissertation for the degree of Doctor of Philosophy.

Reza Abbaschian
Professor of Materials Science and Engineering

I certify that I have read this study and that in my opinion it conforms to acceptable standards of scholarly presentation and is fully adequate, in scope and quality, as a dissertation for the degree of Doctor of Philosophy.

Robert T. DeHoff
Professor of Materials Science and Engineering

I certify that I have read this study and that in my opinion it conforms to acceptable standards of scholarly presentation and is fully adequate, in scope and quality, as a dissertation for the degree of Doctor of Philosophy.

Fereshteh Ebrahimi
Associate Professor of Materials Science and Engineering

I certify that I have read this study and that in my opinion it conforms to acceptable standards of scholarly presentation and is fully adequate, in scope and quality, as a dissertation for the degree of Doctor of Philosophy.

Ashok V. Kumar
Assistant Professor of Mechanical Engineering

This dissertation was submitted to the Graduate Faculty of College of Engineering and to the Graduate School and was accepted as partial fulfillment of the requirements for the degree of Doctor of Philosophy .

May, 1997

Winfred M. Phillips
Dean, College of Engineering

Karen A. Holbrook
Dean, Graduate School